Modeling and Characterization of Millimeter-wave Photodiodes for Microwave Photonic Integrated Circuits

A Major Qualifying Project
Submitted to the Faculty of
Worcester Polytechnic Institute
in partial fulfillment of the requirements for the
Degree in Bachelor of Science
In Physics
By

Erin Mae Morissette

Date: 12/11/18

Sponsoring Organization:
MIT Lincoln Laboratory, Lexington MA
Project Advisors:

Professor Douglas Petkie, WPI

Dr. Sivasubramaniam Yegnanarayanan, MIT LL

Abstract

There is worldwide interest in utilizing the millimeter-wave sub-millimeter-wave bands of the electromagnetic spectrum (high frequency microwaves) for high-speed and high-capacity free-space communication systems. Important to this effort is an efficient conversion from the fiber-based optical communications systems to free-space microwave systems. A critical component of these systems is the photodiode, a type of photodetector that receives photons and converts them into photocurrent by means of the photoelectric effect, connecting the optical and microwave domains. This project involved the characterization and modeling of state-of-the-art photodiodes fabricated at MIT Lincoln Laboratory in the Quantum Information and Integrated Nanosystems Group. A preliminary literature review correlated photodiode design with the optimization of speed (3-dB bandwidth), efficiency (responsivity), and power (current-handling). The measurement of the responsivity (the ratio of generated photocurrent to input optical power) as a function of wavelength revealed unexpected oscillations in the responsivity as a function of device length caused by a reflective cavity in the photodiode, resulting in the recommendation of the addition of an anti-reflective coating that eliminated the oscillations. Characterization of current-handling and responsivity demonstrated that the photodiodes could be fabricated to improve overall performance and realize a high-power, high-speed device for microwave photonics applications.

Acknowledgements

First, I would like to thank my main advisor, Douglas Petkie, for all of his guidance and the many hours spent reading and editing.

I would also like to thank my advisors at MIT Lincoln Laboratory, Siva Yegnanarayanan, Jason Plant, Cheryl Agaskar, and Paul Juodawlkis for the invaluable insight and countless learning opportunities they offered.

I would like to thank Alex Mederios and Ryan Maxson for their help and patience in the Integrated Photonics Lab at MIT LL.

I would like to thank Barbara Santorella and John Bilodeau at MIT LL for their technical support.

I would like to thank the members of the MIT LL Group 89 program this project was a part of: Siva Yegnanarayanan, Jason Plant, Chris Heidelberger, Cheryl Agaskar, Dave Kharas, Wayne Woods, Terence Weir, Ryan Maxson, and Paul Juodawlkis.

I would like to thank the project site organizers: George Heineman (WPI), Edward Clancy (WPI), Brett Levasseur (MIT LL), Kathleen Nahabedian (MIT LL), and Sarah Curry (MIT LL).

Finally, I would like to thank the other WPI MQP students at MIT LL for their general support, feedback, and camaraderie.

Table of Contents

1. Introduction

The increasing demand of high-performing communication systems within both defense and commercial areas necessitates advancement of receiver/transmission technology. Currently, there is worldwide interest in utilizing the millimeter-wave and sub-millimeter-wave bands of the electromagnetic spectrum (high frequency microwaves). This band of the frequency spectrum, ranging from 30 – 300 GHz, is advantageous for data transfer, particularly in terms of spectrum availability as well as device Size, Weight, and Power (SWaP). However, the increased free-space path loss (FSPL) and considerable atmospheric attenuation of microwaves pose challenges to the accessibility of this part of the spectrum. Therefore, innovative technology must be incorporated into antennas and receiver devices in order to develop high power, low noise millimeter-wave systems.

The interdisciplinary field of microwave photonics (MWP), in which optoelectronic components are integrated into transmitters and receivers, has emerged as a leading candidate in the effort of realizing optimal, high-frequency systems. When compared to microwave techniques alone, optical components are considered more robust to electromagnetic interference and hence favorable for secure communication systems [2]. MWP employs the strengths of photonic integrated circuits (PICs) to convert light signals into electric current that can be further manipulated in different ways depending on the desired application [3]. Applications of MWP systems include phased array antennas, radio-over-fiber links, terahertz (THz) signal generation, and ultra-broad-band wireless communication – all of which offer extraordinary benefits in medical, commercial, and defense interests.

In all of these applications, a critical component of the system is the photodiode. A photodiode is a type of photodetector that receives photons and converts them back into electrons by means of the photoelectric effect [7]. Therefore, the role of the photodiode in these systems is converting optical signal to electrical signal. In high-performing MWP systems, the photodiode must have a large bandwidth, high saturation photocurrent, and high external responsivity. While these metrics have been individually demonstrated in existing photodiodes, they have yet to be achieved simultaneously and with the relatively simple array integration necessary for MWP systems. Toward this effort, the Quantum Information and Integrated Nanosystems Group (89) at MIT Lincoln Laboratory has designed and fabricated InGaAs/InP evanescently-coupled

waveguide modified uni-traveling-carrier (MUTC) variable-confinement slab-coupled optical photodiodes (VC-SCOWPDs) for chip-scale, microwave photonic integrated circuits (MWPICs).

The goal of this project is to model and fully characterize the photodiodes fabricated by Group 89 in the effort to further understand the mechanisms by which these devices can operate at high speed and power for integration into MWP systems. In order to accomplish this goal, the project consists of the following objectives:

1. Understand relevant device physics concepts such as Maxwell's equations, optical properties of semiconductor materials, and electron/hole transport in III-V hetero-structures, as well as how these concepts will manifest in device testing.
2. Perform DC device tests to characterize the following parameters of the fabricated UTC-PDs: IV curves and dark currents, optical external responsivity, and saturation photocurrent.
3. Develop a theoretical model for optical propagation through the fabricated material structure to compare with measured results and eventually inform future design recommendations.

Together, these objectives will allow the investigation to exhaustively compare theoretical performance according to device physics, past device performance reported in the literature, and measured performance from Group 89's InGaAs/InP photodiodes.

The next chapters include background material for photodiode physics, a literature review detailing the current state of the technology, detailed methodology of the project, presentation of the collected data, and discussion of the results.

2. Background

The first section of this chapter presents the relevant background and motivation for millimeter-wave technology and microwave photonic (MWP) systems. The second section details the device physics concepts involved in the operation and testing of photodiodes. This will include varying designs and material structures, illustrating the current state of InP-based photodiode technology with highlights from the project's literature review. The third and final section will detail the specifications of the photodiodes fabricated by Group 89 at MIT Lincoln Laboratory.

2.1.1 Millimeter waves

The millimeter-wave and sub-millimeter-wave bands of the electromagnetic spectrum, also identified as high-frequency microwaves, have recently garnered interest for applications in communication systems. Given the anticipated levels of wireless network congestion in the near future, accessing this part of the spectrum is a possible solution for larger bandwidth availability. The millimeter-wave band ranges from 30-300 GHz, and is advantageous for data transfer as well as device Size, Weight, and Power (SWaP) due to higher frequencies and shorter wavelengths (Figure 2-1, below).

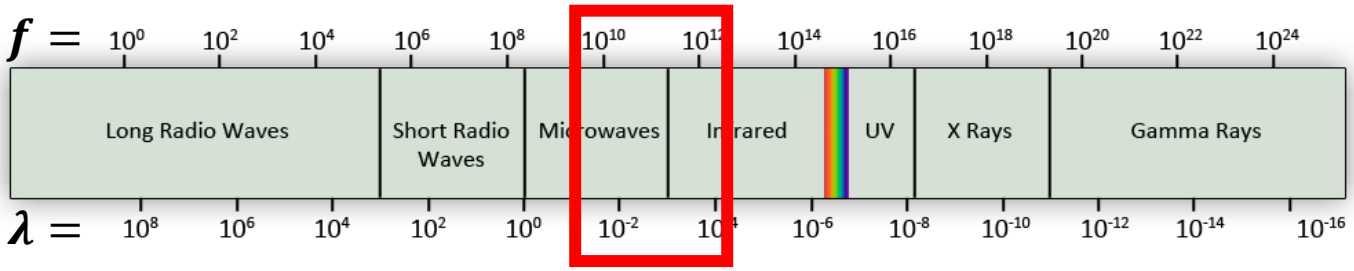

Figure 2-1: The electromagnetic spectrum, with frequencies labeled on the top in Hertz (Hz), and wavelength labeled on the bottom in meters (m). The red box roughly outlines the millimeter-wave and sub-millimeter wave bands of the spectrum, also known as high-frequency microwaves [modified from 12].

Microwaves with higher frequencies allow for increased data transfer speed and communication, and shorter wavelengths allow for smaller antenna dimensions given a fixed gain. However, there are substantial challenges that microwave technology must address in order to efficiently generate and receive millimeter waves.

One of the most prevalent challenges with the millimeter-wave band of the spectrum is transmission and propagation efficiency. Propagation between antennas is typically described by the Friis transmission equation:

$$\frac{P_r}{P_t} = e_r e_t \left(\frac{\lambda}{4\pi R}\right)^2 D_r D_t = \left(\frac{\lambda}{4\pi R}\right)^2 G_{0r} G_{0t} \tag{2-1}$$

in which P is power, e is antenna efficiency, λ is electromagnetic wavelength, R is distance between the antennas, D is the directivity of the antenna relative to isotropic, G is the antenna gain ($G = eD$), and subscripts r and t represent receiver and transmitter, respectively [11]. Derived from the Friis transmission equation is the free-space path loss (FSPL) equation:

$$FSPL = \left(\frac{4\pi R}{\lambda}\right)^2 \tag{2-2}$$

Since wavelength is inversely proportional to free-space path loss, shorter wavelengths such as microwaves will experience greater loss in free space compared to longer wavelengths such as radio waves. Additionally, this equation illustrates ideal conditions under which waves propagate, such as satellite communication in space where there is negligible atmospheric absorption and no ground reflections. Free-space path loss increases when variables such as atmospheric absorption and obstructions such as buildings are introduced.

Millimeter-wave signals experience considerable levels of attenuation due to atmospheric absorption (see Figure 2-2 below). For long-range communication systems, “windows” of lower attenuation between oxygen or water peaks must be utilized as the center wavelength/frequency. Three fiber-optic communication bands occur at wavelengths of 0.85, 1.31, and 1.55 μm. As illustrated in Figure 2-3, Rayleigh scattering ($\propto 1/\lambda^4$) decreases with increasing wavelength, therefore the band with the least amount of attenuation and scattering is 1.55 μm, or 1550 nm. Coincidentally, Erbium-doped fiber amplifiers (EDFAs) operate within a range of 1530-1565 nm and exhibit gain at 1550 nm. For these reasons, 1.55-μm optoelectronic devices are a popular choice for communication systems and the center wavelength for Group 89’s devices.

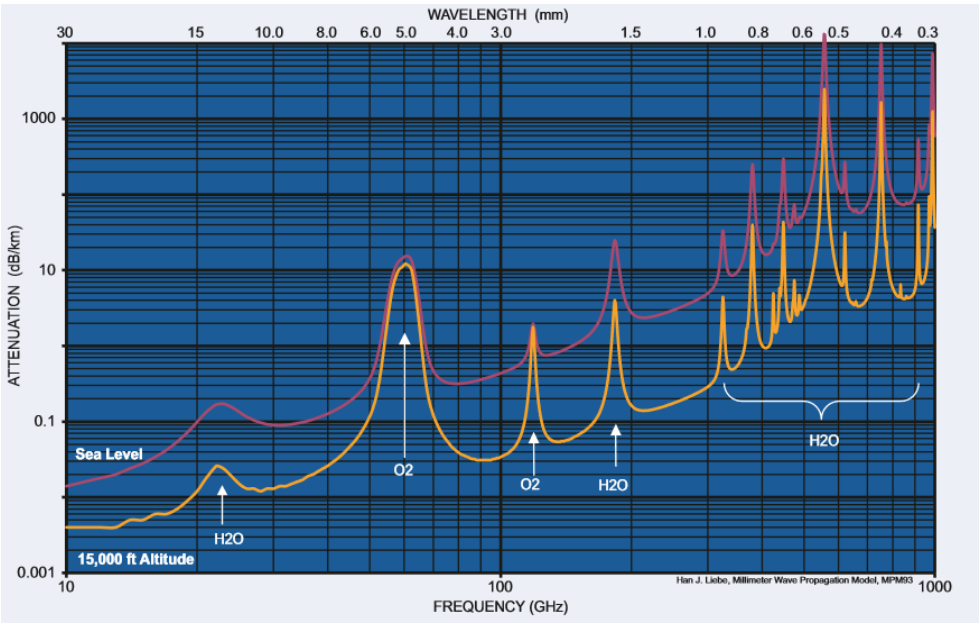

Figure 2-2: Average atmospheric absorption of millimeter waves. Attenuation (dB/km) at sea level denoted by pink line (top), and 15,000 ft. altitude by yellow line (bottom) [1].

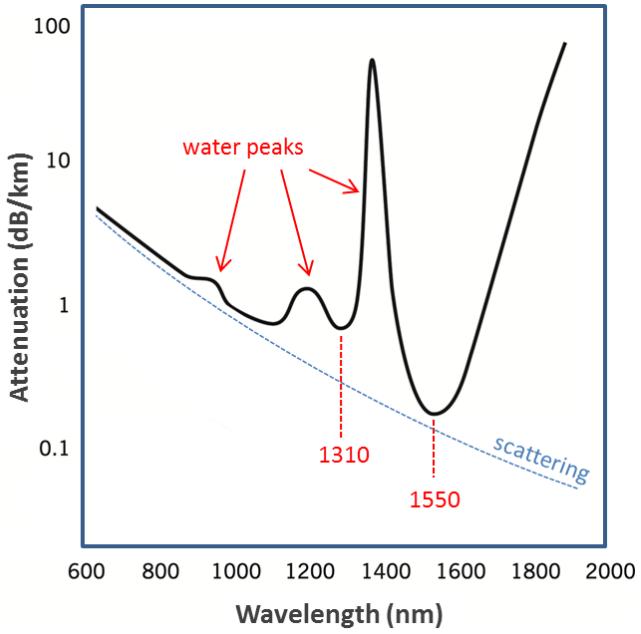

Figure 2-3: Fiber attenuation on the micron-wavelength scale showing communication "windows" at 0.85, 1.31 and 1.55 μm.

2.1.2 Microwave Photonic Systems

The interdisciplinary field of microwave photonics (MWP), in which optoelectronic components are integrated into transmitters and receivers, has emerged as a leading candidate in

the effort of realizing optimal, high-frequency systems. When compared to microwave techniques alone, optical components are considered more robust to electromagnetic interference and hence favorable for secure communication systems [2]. MWP employs the strengths of photonic integrated circuits (PICs) to convert light signals into electric current that can be further manipulated in different ways depending on the desired application [3].

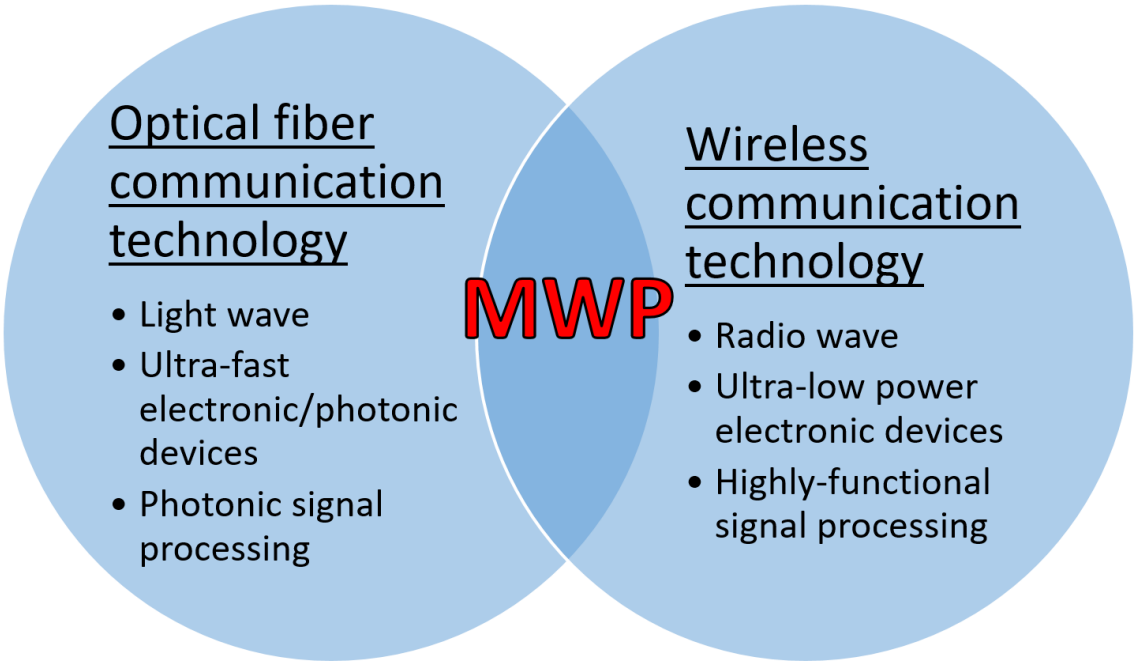

Figure 2-4: A Venn diagram describing microwave photonics (MWP) as the intersection between optical fiber and wireless communication technology and their respective benefits [modified from 4].

The block diagram in Figure 2-5 (below) illustrates an example of the optoelectronic signal conversion process in a 120-GHz-band wireless link. The original data signal and the millimeter-wave-generated signal enter the optical modulator at a rate of 10 Gigabytes/second (Gb/s) to send the modulated, optical data signal to the photodiode (PD) with an amplifier. The photodiode then converts this optical signal to electrical signal that is sent wirelessly at a carrier frequency of 125 GHz to the receiver, which finally recovers the original data signal.

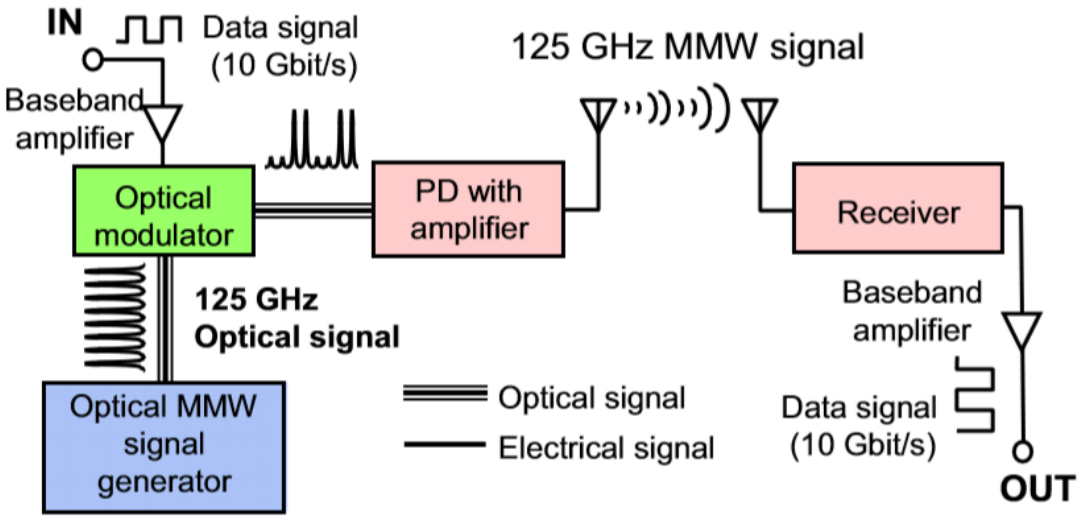

Figure 2-5: A block diagram of a microwave photonic (MWP) wireless link, in which an initial data signal is converted from optical to electronic by a photodiode with an amplifier [4].

Another example of a microwave photonic system application is a phased array antenna, in which optical links are the "backbone" of the structure [2]. In phased array antennas, beam steering is electronically controlled by manipulating the phase of the transmitters, subsequently creating constructive and destructive interference. The receivers utilize the same concept to filter light (the millimeter-wave signal) from a defined direction [2]. The concept of microwave photonic integrated circuits (MWPICs) incorporates the MWP system technology at a chip-size scale to allow for optimal portability and power consumption required in, for example, military environments. Additional applications of microwave photonic systems are radio-over-fiber links, terahertz (THz) signal generation, and general "ultra-broad-band" wireless communication [5, 6].

2.2 Photodiode Physics and Technology

In all of these applications, a critical component of a high-performing MWP system is the photodiode. A photodiode is a type of photodetector that receives photons and converts them back into electrons by means of the photoelectric effect [7]. Therefore, the role of the photodiode in these systems is converting optical signal to electrical signal. There are many different

structures and designs of photodiodes that result in favorable characteristics for integration into MWP systems and MWPICs.

2.2.1 p-i-n Photodiodes

The type of photodiodes used in most PICs today operate with a reverse-biased p-i-n structure. In a p-i-n structure, an unintentionally doped (UID) intrinsic region ("i") acts as the absorber between a p-doped and n-doped layer (see Figure 2-6, below).

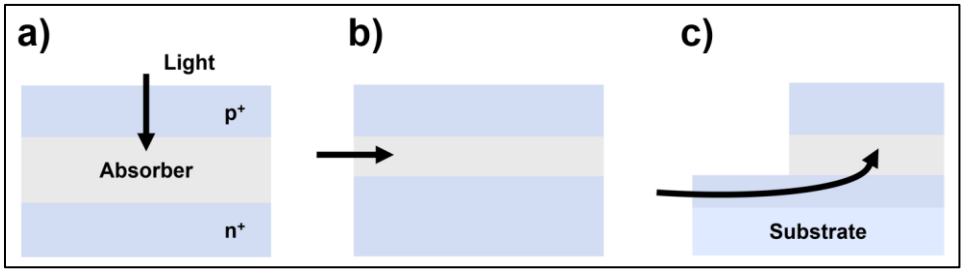

Figure 2-6: (a) Vertically-illuminated photodiode (VPD), (b) side-illuminated waveguide photodiode (WG-PD), and (c) evanescently-coupled WG-PD [modified from 3].

Photodiodes are also classified by how they are illuminated, the simplest of which is the vertically-illuminated photodiode (VPD) in Fig. 5a. The side-illuminated waveguide photodiode (WG-PD) shown in Fig. 5b places the input optical waveguide adjacent to the absorber layer. Lastly, when the photodiode is placed on top of a passive waveguide, it is known as an evanescently-coupled WG-PD as shown in Figure 2-6(c).

In a p-i-n photodiode, photons enter the absorber layer and create electron-hole pairs that separate to travel in opposite directions along the conduction and valence bands, respectively (see Figure 2-7, below). The electron-carriers generated from the photons manifest as current in the photodiode (referred to as photocurrent), and the speed at which these carriers travel through the absorption layer directly influences the performance of the device. Therefore, the intrinsic characteristics of the semiconductor materials, such as bandgap and electron/hole velocity, are a critical aspect in photodiode design.

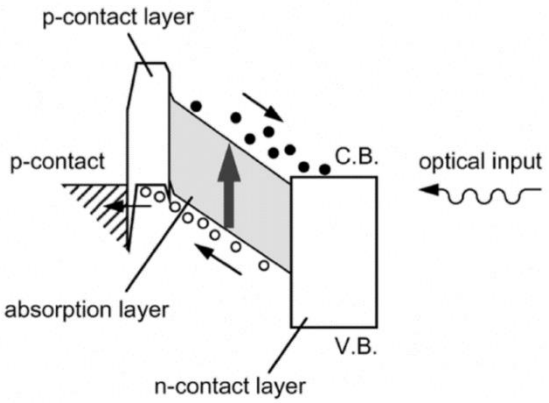

Figure 2-7: Band structure diagram of a p-i-n photodiode in which "C.B." denotes the conduction band and "V.B." denote the valence band.

2.2.2 III-V Material Growth and InGaAs/InP Photodiodes

The most common methods of high-quality, semiconductor multi-layer structure fabrication is epitaxial growth via molecular beam epitaxy (MBE) or metal-organic chemical vapor deposition (MOCVD, also referred to as MOVPE). In MOCVD growth of III-V materials, organometallic liquids (triethylindium, triethylgallium) and hydride precursors (arsine, phosphine) saturate an H_2 carrier gas at temperatures around 600°C to create the desired semiconductor and a gas byproduct [7]. An example of this process is the reaction to create GaAs:

$$Ga(CH_3)_3 + AsH_3 \rightarrow \mathbf{GaAs} + 3CH_4 \qquad (2\text{-}3)$$

Currently, the materials believed to be most suitable for fabricating high-power, high frequency optoelectronic devices are InP, a III-V semiconductor with a direct band gap of 1.35 eV, and its lattice-matched, compound semiconductors InGaAs, InGaAsP, and InAlGaAs (see Figure 2-8, below). $In_{0.53}Ga_{0.47}As$ specifically has an absorption coefficient of 7000 cm^{-1} at 1.55 μm, an important communication wavelength as discussed in Section 2.1.1 and the center wavelength of the devices of interest [3]. Group 89 employs an AIXTRON vertical chamber reactor for III-V MOCVD growth on two-inch, InP substrate wafers. Dopants in the structures are deposited in-situ, and the elements are zinc for p-type doping and silicon for n-type doping.

In addition to a direct band gap, the advantage of InP is an intrinsic electron mobility of 5400 $cm^2 \cdot V^{-1} \cdot s^{-1}$ – much higher than other semiconductors such as Si ($\leq$1400 $cm^2 \cdot V^{-1} \cdot s^{-1}$). The composite $In_{0.53}Ga_{0.47}As$ is the most relevant in photodetector devices – it is often utilized as the

absorber material due to its high electron mobility of 10,000 $cm^2 \cdot V^{-1} \cdot s^{-1}$ and corresponding electron drift velocity of 6.5×10^6 cm/s [3]. In photodiodes, higher drift velocities of the carriers in the absorber correspond to higher device speed.

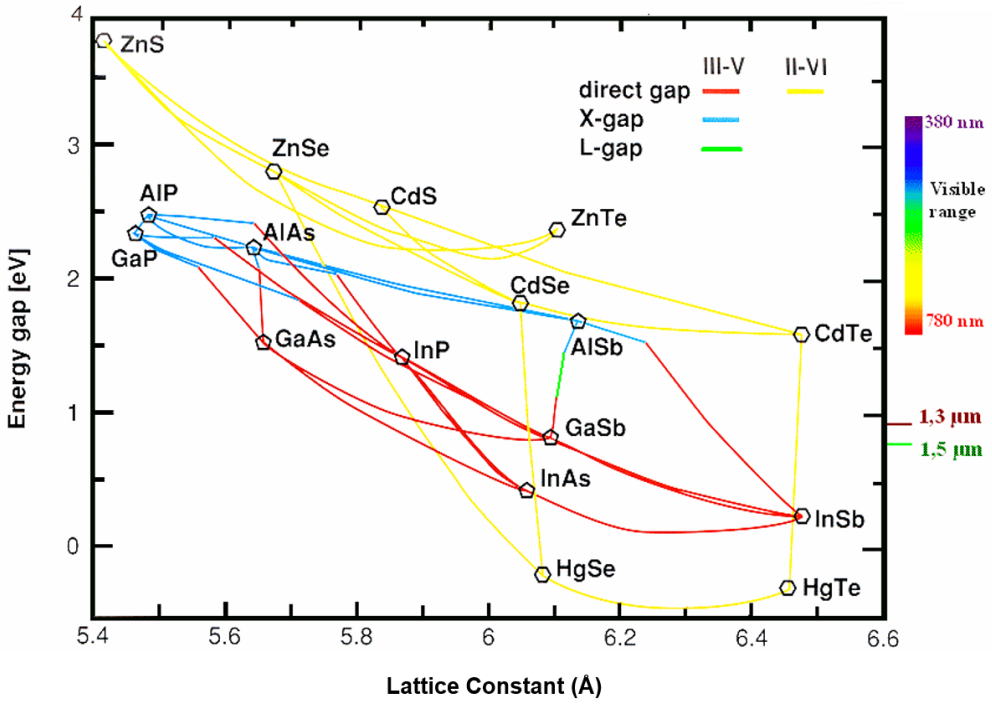

Figure 2-8: Graph of energy gap (eV) as a function of lattice constant (Å) for III-V and II-VI binary semiconductors. Wavelengths corresponding to energy gaps are displayed on the right axis [13].

2.2.3 Photolithography

Following the epitaxial growth of the material, the structures of the photodiodes and waveguides are realized with photolithography. The practice of photolithography (also referred to as optical lithography) generally involves the following steps:

- Spin-coat the wafer with photoresist – a light-sensitive material
- Align the wafer to a mask (akin to a stencil) of a specified design
- Expose the wafer to UV light
- Develop the wafer in photoresist developer

With a positive photoresist, the area exposed to the UV light (not covered by the mask) becomes soluble to the developer, and the wafer is left with the pattern on the mask. With a negative

photoresist, the area exposed to UV light becomes resistant to the developer, and the wafer becomes a negative of the mask pattern. This process has traditionally been done using a physical quartz mask. Physical masks allow for consistent, sub-micron alignment accuracy, but the alignment process is arduous and ordering the masks is expensive and time-consuming. New techniques include a "mask-less aligner" (MLA) that directly writes the pattern onto the wafer with lasers. The MLA allows for rapid mask design and modification, but the process is not yet as dependable as manual alignment.

The next step of realizing mesas from the material stack is vertical etching, either by wet (chemical) or dry (reactive-ion or inductively-coupled plasma) etching. In both wet and dry etching, layers of the material are selectively removed from the stack in patterns determined by the remaining photoresist. For example, to create a mesa in a multi-stage slab-coupled optical waveguide amplifier (SCOWA), the top InP cap layer and InGaAsP vertical taper (VT) layer must be removed from certain areas of the wafer (see Figure 2-9, below).

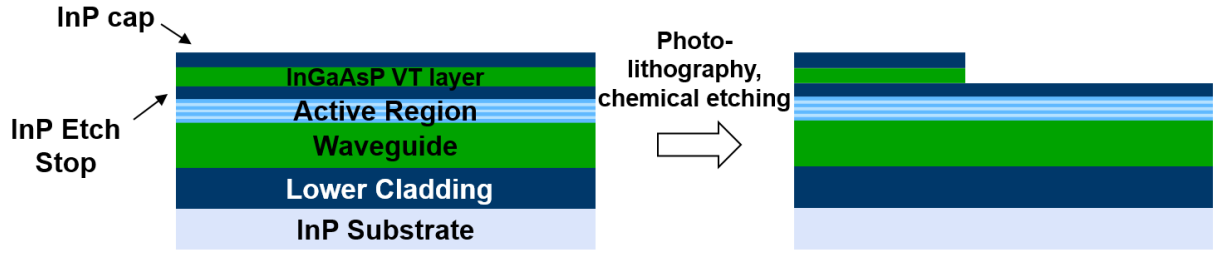

Figure 2-9: An example of photolithography in which wet etching is used to selectively remove first the InP cap layer with and then the InGaAsP VT layer.

To remove the InP cap layer, the wafer is dipped in 1:1 HCl:H_3PO_4 for 30 s. The hydrochloric-phosphoric solution only reacts with the InP to dissolve it away at a rate of 2 μm/min, but it does not react with the InGaAsP layer below it – hence the solution is selective to InP from InGaAsP. Analogously, a dilute piranha solution (1:1:10 – H_2SO_4:H_2O_2:H_2O) is used to selectively remove the InGaAsP VT layer from the InP etch stop. Dry etching via inductively-coupled plasma (ICP) is achieved by generating high-density plasma with an RF-magnetic field that chemically (and mechanically) reacts with the material to selectively remove it. Wet etching is often faster, but dry etching is generally more consistent.

Once the structures are defined on the wafer, the photoresist is removed and n/p-type metals are deposited to achieve ohmic contacts. Ohmic contact occurs when an electrical junction has a linear current-voltage response (Ohm's Law: V=IR), as opposed to Schottky barriers that do not behave linearly. Finally, rapid thermal annealing is performed at high temperatures to secure the metal onto the wafer. Spatially precise photolithography and fabrication is a critical aspect of the development of high-performing photodiodes.

2.2.4 Performance metrics of photodiodes

In order to characterize the performance of photodiodes, the RF bandwidth, external responsivity, saturation characteristics, dark current, polarization dependence, and linearity of the device must be measured. Bandwidth is the range of frequencies over which a photodiode can receive a signal (at a specified performance level). A more specific measure of bandwidth for photodiodes is 3-dB bandwidth, denoted f_{3dB}. 3-dB bandwidth is the upper frequency limit at which the relative power drops by 3 dB (see Figure 2-10). External responsivity is the ratio of photocurrent to input power, or the ratio of generated electrons to incident photons. Therefore, responsivity is directly proportional to quantum efficiency:

$$R = \frac{I_p}{P_{in}} \propto \eta \qquad \eta = \frac{P_{in} - P_t}{P_{in}} = 1 - e^{-\alpha L} \tag{2-4}$$

where R is external responsivity, I_p is photocurrent, P_{in} is input power, η is quantum efficiency, P_t is transmitted power, α is absorption coefficient of the absorber material, and L is the thickness of the absorber [3].

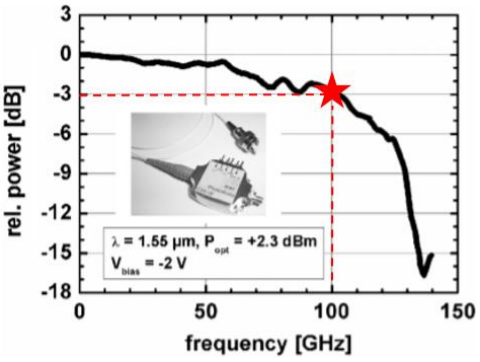

Figure 2-10: An example of a photodiode with 100 GHz 3-dB bandwidth (3-dB intersection denote by star).

Saturation characteristics include saturation photocurrent or RF output power at a given frequency. Either metric describes the point at which the device begins to saturate and deviate from ideal current-power behavior. Dark current is a measure of current as a function of voltage when the device is not photo-excited, and values on the order of 10^{-7} – 10^{-9} Amperes indicate negligible amounts of reverse-bias leakage current in the device. Polarization-dependent loss (PDL = $10\log(R_{TE}/R_{TM})$) measures the loss in dB that arises from varying polarizations of the incident light from the fiber, and lower values are preferable to preserve signal quality [5]. Lastly, linearity is characterized by the third-order intercept point (OIP3) in dBm in which higher intercepts indicate a more linear device, favorable in signal processing. Metrics of RF bandwidth, responsivity, and saturation photocurrent will be the focus of this work.

For efficient integration into high-performing MWPICs or other MWP systems, photodiodes should ideally have a 3-dB bandwidth of 60-100 GHz, external responsivity of > 0.5 A/W, and total saturation photocurrent of 40-100 mA (depending on whether the system design includes arrays of multiple photodiodes). Existing photodiodes have met one or two of these metrics simultaneously, but a single device has yet to meet all three performance characteristics with relatively simple array integration capabilities. A significant challenge in achieving high bandwidth, responsivity, and saturation photocurrent simultaneously is the tradeoff between the three metrics as a function of device active area and absorber thickness. The total 3-dB bandwidth of the device consists of two components: transit-time limited bandwidth, and resistance-capacitance (RC)-limited bandwidth. Transit-time limited bandwidth can be calculated by the following equation:

$$f_t \cong \frac{0.44\, v_{sat}}{d} \tag{2-5}$$

where f_t is the transit-time limited frequency/bandwidth, $v_{sat}$is the saturated carrier velocity in the absorption region (~ 7×10^6 cm/s for InGaAs), and d is the absorber thickness [8]. Since absorber thickness is inversely proportional to f_t, a thicker layer increases the carrier transit time and subsequently limits the bandwidth. However, RC-limited bandwidth is directly proportional to absorber thickness:

$$f_{RC} \cong \frac{1}{2\pi C(R_s + R_L)} \qquad C = \frac{A\varepsilon_0\varepsilon_r}{d} \tag{2-6}$$

where C is the diode capacitance, R_s is the series resistance, R_L is the load resistance (typically 50 Ω), A is the active area of the device, ε_0 is the permittivity of free space, and ε_r is the relative permittivity of the absorber material (12 for InGaAs). Therefore, a thicker absorber layer will increase the RC-limited bandwidth. The total 3-dB bandwidth can be approximated by the following combination of transit-time and RC-limited bandwidths:

$$\frac{1}{f_{3dB}^2} \cong \frac{1}{f_t^2} + \frac{1}{f_{RC}^2} \tag{2-7}$$

Substituting the previous equations yields an equation for the total bandwidth of a p-i-n vertically-illuminated photodiode (VPD), with contours plotted in Figure 2-11, below.

$$f_{3dB} = \frac{1}{\sqrt{\left(2\pi[R_s + R_L]\frac{A\varepsilon_0\varepsilon_r}{d}\right)^2 + \left(\frac{d}{0.44\, v_{sat}}\right)^2}} \tag{2-8}$$

As can be seen in the bandwidth contours in Figure 2-11 (below), bandwidth increases as the active area of the photodiode decreases. However, the responsivity of the device also decreases since there is a smaller area for incident photons to be absorbed. Therefore, there is a tradeoff between RF bandwidth and responsivity due to active device area.

In waveguide photodiodes (WGPDs, Fig. 2-6(b-c), however, bandwidth and responsivity become somewhat decoupled. This is because bandwidth is dependent on intrinsic layer thickness, while responsivity depends on absorption length and input coupling efficiency. Decoupling the tradeoff present in VPDs allows for an improved bandwidth-efficiency product in WGPDs.

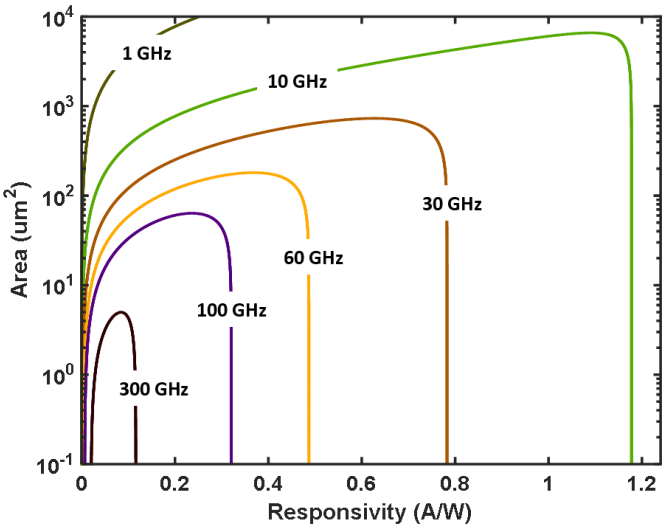

Figure 2-11: Bandwidth contours for a surface-illuminated p-i-n photodiode (VPD) as functions of area and responsivity. With increasing bandwidth, active device area (μm^2) as well as responsivity (A/W) decreases.

2.2.5 Literature examples of p-i-n photodiodes

In the effort to develop high-speed photodiodes for 40-Gb/s applications, Achouche *et al.* [8] designed and fabricated several InGaAs/InP evanescently-coupled waveguide p-i-n photodiodes. The material structure, illustrated in Figure 2-12, includes an undoped, 400-nm InGaAs absorber between an n-InGaAsP optical matching layer and a p-InP mesa layer.

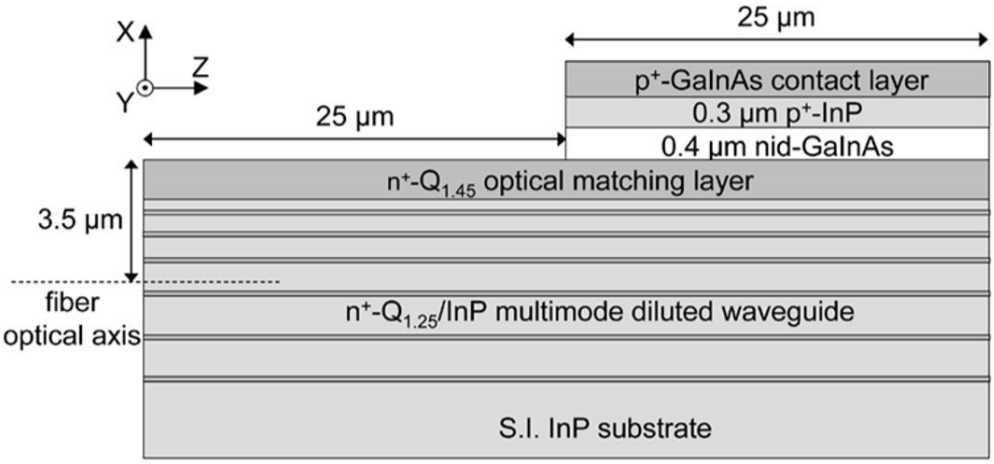

Figure 2-12: The material structure of an InGaAs/InP evanescently-coupled p-i-n photodiode and multimode diluted waveguide. "nid" indicates nonintentionally doped, $Q_{1.25}$ refers to InGaAsP with bandgap $\lambda_g = 1.25\ \mu$m, and $Q_{1.45}$ InGaAsP with $\lambda_g = 1.45\ \mu$m [8].

To determine the optimal length of the device, they calculated the 3-dB bandwidth as a function of length utilizing the 3-dB bandwidth equation and holding the width/absorber thickness constant at 5 μm and 400 nm, respectively. According to the analytical model results and corresponding measurements, a length of 25 μm would simultaneously allow for a bandwidth of 48 GHz and high responsivity. The measured 3-dB bandwidth, responsivity, and device area is shown in Figure 2-13, below:

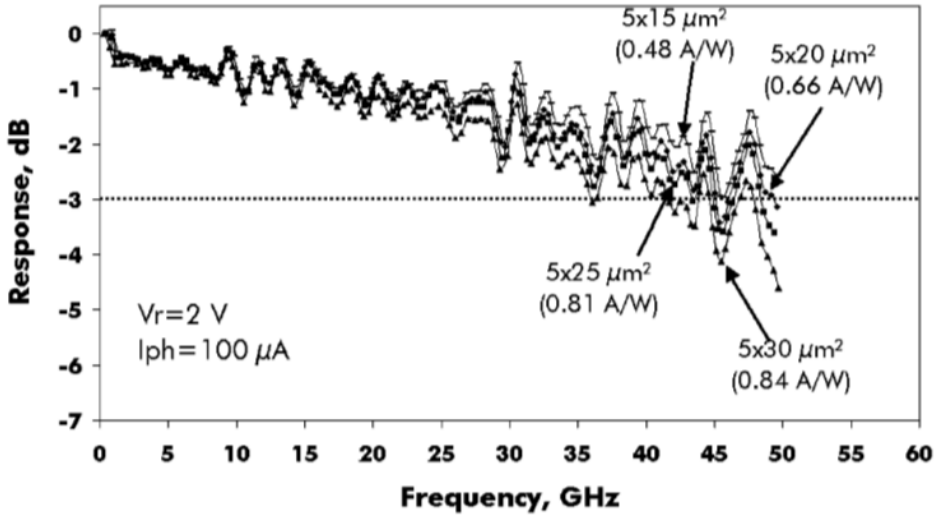

Figure 2-13: Normalized response (dB) as a function of frequency (GHz) displaying 3-dB bandwidth (frequency at which signal crosses the -3-dB line) with labeled device area and responsivity. The 5×25 μm^2 device had a responsivity of 0.81 A/W and a 3-dB bandwidth of 47 GHz [8].

In the fabrication of the device, a SiN_x passivation layer was deposited by chemical vapor deposition (CVD) to act as an antireflective (AR)-coating layer. AR-coating increased the external responsivity of the device by reducing insertion loss and minimizing the back-reflected light in the cavity. The material of the AR-coating layer was chosen such that the index of refraction and thickness results in destructive wave interference, governed by Fresnel's equations for the transmission and reflection of light.

While the 5×25 μm^2 device had favorable performance metrics for RF bandwidth (f_{3dB}= 47 GHz) and external responsivity (R = 0.81 A/W), the average saturation photocurrent was limited at 11 mA for 40 GHz. Larger devices had increased saturation photocurrent, but a lower bandwidth of 42 GHz. However, the group determined that optimized bandwidth and external responsivity of the device would yield "high performance operation at 40 Gb/s."

Bach *et al.* in [9] designed a similar waveguide-integrated p-i-n photodiode but with an increased 3-dB bandwidth of 100 GHz. The material stack was grown via one-step MOVPE and included a 420-nm thick InGaAs absorption layer (Layer 5 in Figure 2-14, below).

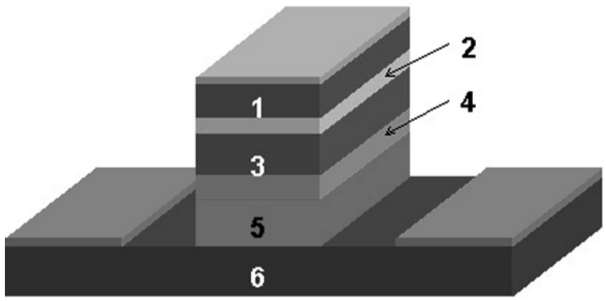

Region	Material	Doping (cm^{-3})
1	InGaAs	$N_A = 1 \times 10^{19}$
2	$InGaAsP_{1.3}$	$N_A = 5 \times 10^{18}$
3	$InGaAsP_{1.15}$	$N_A = 5 \times 10^{17}$
4	$InGaAsP_{1.3}$	$N_A = 1 \times 10^{17}$
5	InGaAs	$N_D = 3 \times 10^{14}$
6	$InGaAsP_{1.33}$	$N_D = 2 \times 10^{18}$

Figure 2-14: Epitaxial growth structure of a waveguide-integrated, p-i-n photodiode in which the InGaAs absorber layer is 420-nm thick and labeled as Region 5. N_A and N_D denote "acceptor" (p-type) and "donor" (n-type) doping, respectively [9].

Due to "deep infusion" of Zinc-doping from the n-type layers above the absorber, the effective space-charge region thickness of the absorber is reduced from 420 nm to 350 nm. Instead of SiN_x, a benzacyclothenebutol (BCB) layer was deposited to passivate the mesa. The design also included an air bridge that coupled the photodiode mesa to the 50-Ω terminating resistor. The 5×20 μm^2 device was characterized with a 3-dB bandwidth of 100 GHz, external responsivity of 0.66 A/W, and a polarization dependent loss (PDL) of 0.9 dB. The authors attribute these performance metrics to the low resistance of the Zinc-diffused top contact, optimized effective absorption layer thickness, and impedance control from the air bridge.

Although the responsivity is lower than the previous work, this device had an increased saturation photocurrent of 22 mA. The RF output power was also measured to be -7 dBm (~ 0.2 mW) at 100 GHz, biased at -2 V. The high bandwidth of the device, in addition to simple

coupling abilities and ± 2 μm misalignment tolerances, shows progress toward a detector chip that obtains Bessel filter characteristics, a filter with favorable signal preservation.

While waveguide p-i-n photodiodes can achieve relatively high-performance in bandwidth and responsivity, photocurrent remains a limiting factor. An important aspect of performance metric tradeoff, specifically concerning saturation photocurrent, is the space-charge effect. The space-charge effect occurs at high current densities (smaller devices) in which a space-charge field is generated by electrons and holes traveling in opposite directions, as in the absorption layer of a p-i-n photodiode shown in Figure 2-7 [3]. Increased optical input power will increase this generated field until the bias electric field collapses; carrier velocities are reduced, transit times are lengthened, and device performance suffers. While decreased active area improves the RC-limited bandwidth, increased current density exacerbates the space-charge effect.

Recently, uni-traveling-carrier photodiodes (UTC-PDs) have been proposed as an alternative to the traditional p-i-n structure to lessen the space-charge effect and subsequently achieve even higher speed and power performance.

2.2.6 Uni-traveling-carrier photodiodes (UTC-PDs)

In uni-traveling-carrier photodiodes (UTC-PDs), only electrons with higher drift velocities are used as active carriers (see Figure 2-15(a), below). This differs from p-i-n structures in which both holes and electrons are active carriers, and the current responds only as fast as the slower-moving holes can travel. In UTC structures, the narrow-bandgap absorption layer is p-doped to enable the holes to respond within the material's dielectric relaxation time [3].

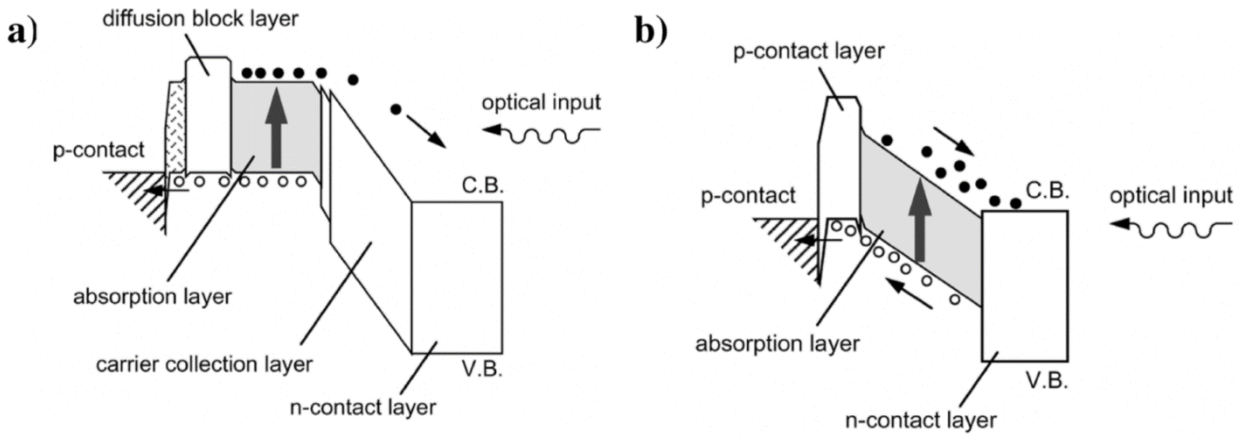

Figure 2-15: Band structure diagram of (a) uni-traveling-carrier photodiode (UTC-PD) and (b) p-i-n photodiode [modified from 7].

Dielectric relaxation is a delay in the response of a dielectric medium in the presence of an external, oscillating electric field. The Debye relaxation equation describes the response of an ideal, non-interacting collection of dipoles to an oscillating electric field as a function of the field's frequency:

$$\hat{\varepsilon}(\omega) = \varepsilon_{\infty} + \frac{\Delta\varepsilon}{1 + i\omega\tau} \tag{2-9}$$

in which ε_{∞} is the permittivity at the high frequency limit, $\Delta\varepsilon$ is the difference between the static low-frequency permittivity and ε_{∞}, and τ is the intrinsic relaxation time of the material.

Electrons are able to reach overshoot velocities as they drift across the un-doped, wide-bandgap carrier collection layer, thereby increasing device speed. Surface-illuminated UTC-PDs have lower quantum efficiency and responsivity because of the thin (~200 nm), p-type absorption layers but as in WG-PDs, edge-coupled waveguide UTC-PDs improve the quantum efficiency and responsivity [14]. For these reasons, waveguide UTC-PDs offer enhanced performance characteristics compared to traditional p-i-n photodiodes.

2.2.6 Literature examples of UTC-PDs

In addition to the p-i-n photodiode first mentioned in section 2.2.5, Achouche *et al.* in [16] designed and fabricated an evanescent edge-coupled waveguide uni-traveling-carrier photodiode (UTC-PD). The structure was grown via molecular beam epitaxy, and included a p-type (~10^{17} cm^{-3}) 200-nm InGaAs absorption layer between a 500-nm p+ InP barrier layer and a 400-nm n- InGaAsP collector layer (λ = 1.3 μm). To find the optimal optical input waveguide length, the authors performed a simulation compromised of a genetic algorithm and a three-dimensional beam propagation method (BPM) simulation tool. The results and actual measurements, shown in Figure 2-16 below, indicate an optimal length of 20 μm.

The disparity in measured responsivity from the model was suspected to be a result of optical loss from roughness on the input facet. A SiN_x-CVD layer was again used to passivate the diode mesa and increase the responsivity. The smallest area diode, 4×15 μm^2, measured a 3-dB bandwidth (at -8 dBm optical power) of 50 GHz with an external responsivity of 0.58 A/W (see Figure 2-17(a)). This response was found to have almost no bias dependence, and the PDL loss was very low at 0.1 dB.

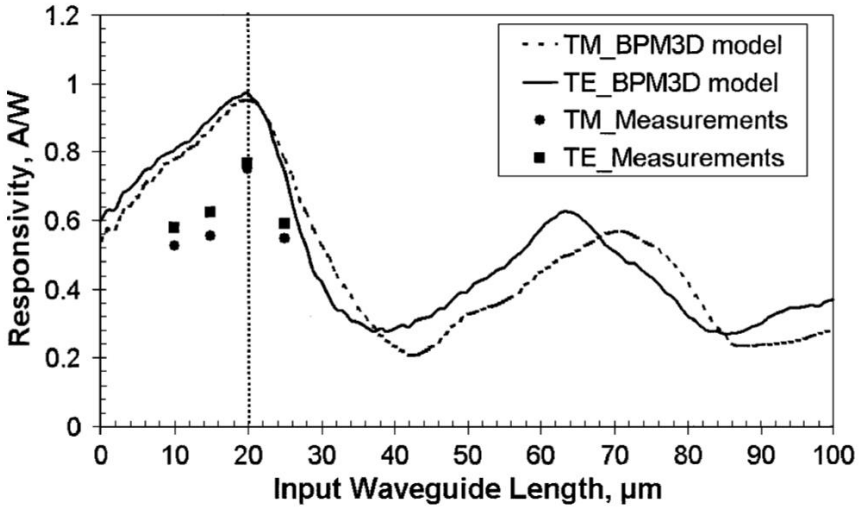

Figure 2-16: External responsivity (A/W) as a function of input waveguide length (μm) from a three-dimensional beam propagation method (BPM3D) model and device measurements [16].

At 10 dBm of optical power (Figure 2-17(b)), the bandwidth and responsivity of the diodes improved. The 4×30 μm^2 device achieved the same bandwidth as the 4×15 μm^2 device (50 GHz) with an increased responsivity of 0.76 A/W.

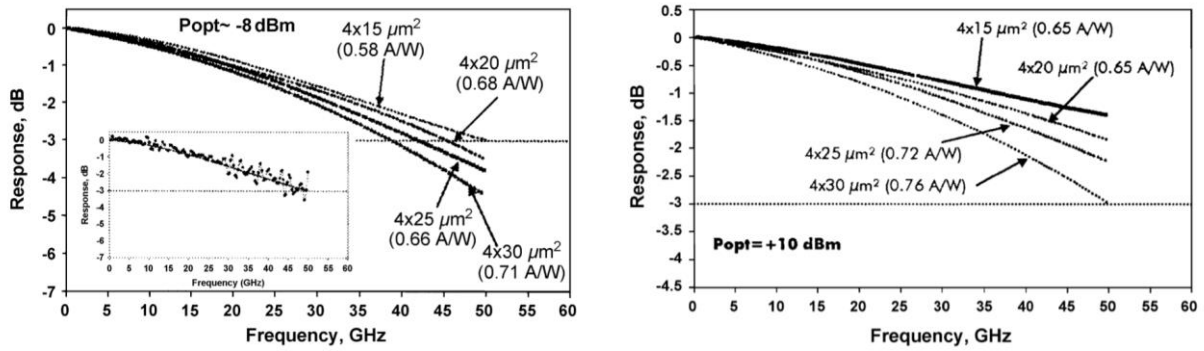

Figure 2-17: (a) Left – frequency response at -8 dBm optical power of 4-μm wide devices at varying lengths of 15, 20, 25, and 30 μm. External responsivities are labeled and 3-dB bandwidth is shown as the frequency that intersects the -3 dB response line. (b) Right – frequency response of the same devices at 10 dBm optical power [16].

Increased bandwidth with increased optical power injection suggested a change of the collector charge state in the absorbent-collector (AC) junction. The total capacitance at that junction is reduced due to the difference between depletion capacitance and differential capacitance ($I_C \times (d\tau_C/dV_{AC})\,|_{W_C}$). Increased responsivity with increased optical power suggested a reduced recombination rate in the p-type absorption layer.

Focused on high-speed devices for microwave photonic integrated circuit (MWPIC) technology, Rouvalis *et al.* in [17] fabricated a coplanar waveguide-integrated UTC-PD chip that consisted of a 2×10 μm^2 active area and a 70-μm long optical input waveguide. These devices achieved a 3-dB of 170 GHz, a responsivity of 0.27 A/W, and an output power of -5 dBm at 170 GHz (see Figure 2-18, below). The authors claimed that at the time of its publishing in 2012, 170 GHz was the highest 3-dB bandwidth demonstrated using active-passive PIC technology. This bandwidth measurement was consistent with RC-limited bandwidth calculations with a series resistance of ~ 40 Ω and a capacitance of ~ 9 fF:

$$f_{RC} = \frac{1}{2\pi[R_s + R_L]C} = \frac{1}{2\pi[40 + 50\ \Omega](9 \times 10^{-15} F)} = 197\ GHz \qquad (2\text{-}10)$$

The low capacitance was a result of the small active area, which translated to a high RC-limited bandwidth.

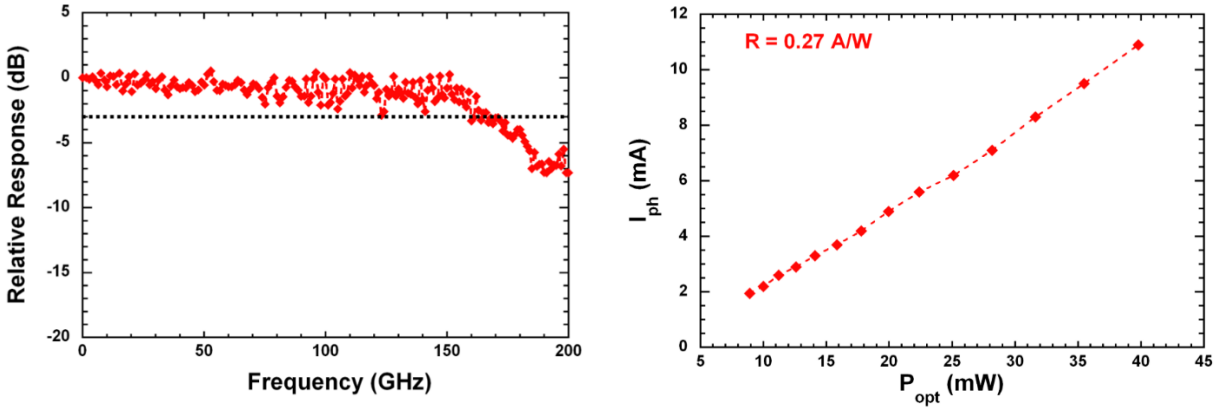

Figure 2-18: (a) Left – Frequency response of a waveguide uni-traveling-carrier (UTC)-PD with active area 2×10 μm^2, exhibiting a 3-dB bandwidth of 170 GHz. (b) Right – photocurrent as a function of optical input power reverse biased at 3 V: $R = I_{ph}/P_{opt}$ = 0.27 A/W, no AR-coating [modified from 17].

The responsivity measurement was taken without AR-coating the device, so it is expected that the responsivity would increase beyond 0.27 A/W with a layer of AR-coating.

The absorber layers in the UTC structure can also be modified to optimize output power while maintaining a high bandwidth. In Zhou *et al.* [5], their modified UTC (MUTC) photodiode contained a 100-nm, n-doped depleted absorber layer toward the substrate in addition to a 100-nm p-type absorber layer (see Figure 2-19, below). The authors claim that the n-doped depleted layer can increase the RF output power by distorting the electric field to compensate for the change imparted by the space-charge effect. To improve electron transport in the p-type absorber layers, the graded doping profile is included to create an additional electric field.

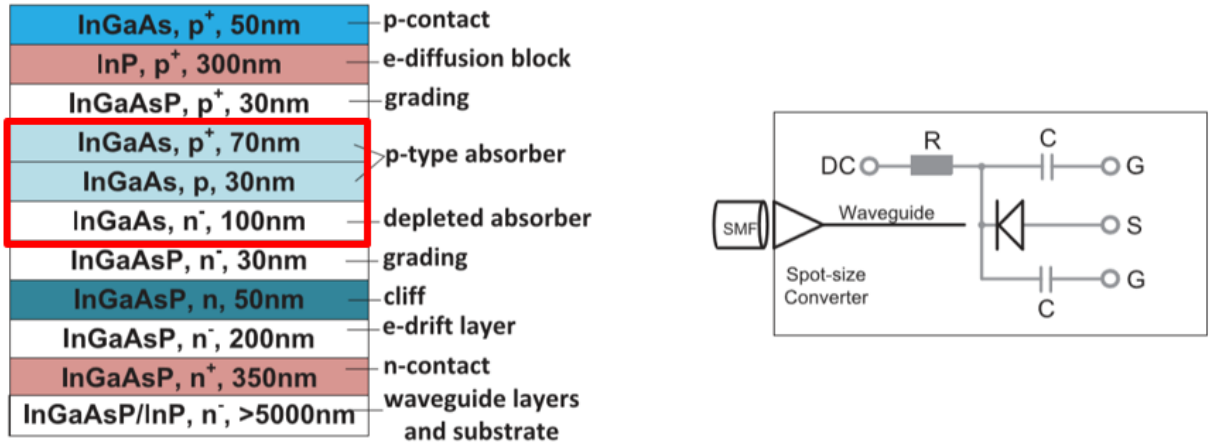

Figure 2-19: (a) Left – Material structure of a modified uni-traveling-carrier (MUTC) photodiode with the absorber layers outlined in red. (b) Right – Optical (black) and electrical (grey) schematic diagram of the waveguide integrated MUTC PD. SMF denotes a single-mode fiber [modified from 5].

At 1550 nm, the MUTC-PD achieved a responsivity of 0.5 A/W (with AR-coating) and a PDL of 0.28 dB. Reversed biased at -2 V, the 3-dB bandwidth of the 4×15 μm^2 device was 75 GHz. At optimal biasing conditions, the RF output power measured 8.9 dBm at 60 GHz and 5.1 dBm at 120 GHz with a 30-mA saturation photocurrent. At the time of the publication, these RF output power measurements were the highest for any reported WGPD.

The work also included results from an array with two photodiodes, called a waveguide-integrated balanced MUTC PD. The pair was monolithically integrated onto one chip with a bias network and a ground-signal-ground (GSG) RF interface. Each PD had a 4×15 μm^2 active area, so the capacitance subsequently doubled and increased the RC time constant. The array measured a 0.5-A/W responsivity, 80-GHz 3-dB bandwidth, and -4.6-dBm RF output power at 105 GHz.

Li *et al.*[6] fabricated similar MUTC-PDs with a focus on high bandwidth and moderate RF output power. Single 24-μm^2 devices measured a 3-dB bandwidth of over 105 GHz (Figure 18b), at a cost of 0.1-A/W responsivity and -4.8-dBm RF output power at 105 GHz. Larger, 50-μm^2 devices achieved an RF output power of 2 and 1.3 dBm at 100 and 105 GHz respectively. The material structure included the same n-doped absorber layer as in [5], but the increase in bandwidth can be attributed to the smaller device size (Figure 2-20(a)).

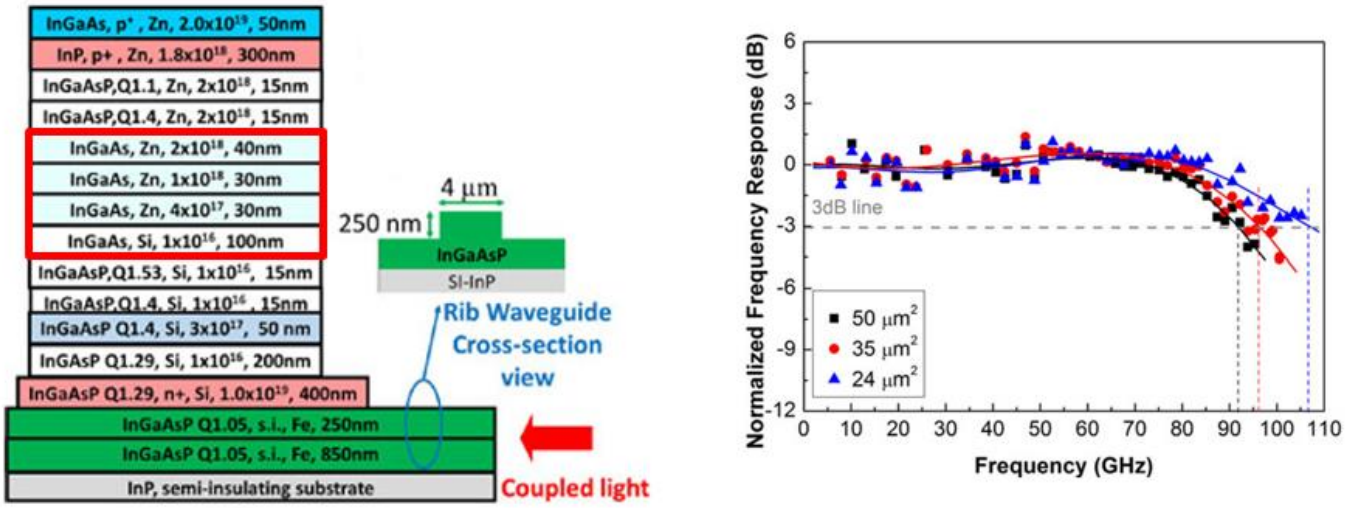

Figure 2-20: (a) Left – Material structure of the modified uni-traveling-carrier (MUTC) photodiode in [6] with absorber layers outlined in red. (b) Right – Frequency response of the 24, 35, and 50 μm^2 devices with bandwidths of 105, 95, and 92 GHz respectively [modified from 6].

2.2.9 Slab-coupled optical waveguide photodiodes (SCOWPDs)

UTC-PDs can also be improved by incorporating control of the mode along the device in the form of variable confinement slab-coupled optical waveguide structures. The optical confinement factor in semiconductor amplifiers and detectors is a measure of the overlap between the optical mode and the active region of the structure:

$$\Gamma = \frac{\iint_{active} |\xi^2| dydx}{\iint |\xi^2| dydx} \tag{2-11}$$

where ξ represents the electric field, and the integral in the numerator is taken over the active region [18]. Waveguide photodiodes are often limited by front-end saturation, an effect where the waveguide area coupled to the optical input becomes saturated before the input power is absorbed down the whole device [19]. To combat this effect, variable confinement structures employ lateral taper mode transformers to change the mode size and confinement factor down the length of the device. At the input of the device, a large mode size and small confinement factor enable lower-loss fiber coupling and low absorption. Therefore, front-end saturation is greatly reduced.

Control of the mode size and absorption profile along the length of a photodiode allow optimization of device speed and power. Klamkin *et al.* demonstrated in [19] uni-traveling-carrier variable-confinement slab-coupled optical waveguide photodiodes (UTC-VCSCOWPD) with high saturation photocurrent and responsivity. Figure 2-21 illustrates the general material structure of the device as well as the simulated absorption profiles of conventional WGPDs and UTC-VCSCOWPDs.

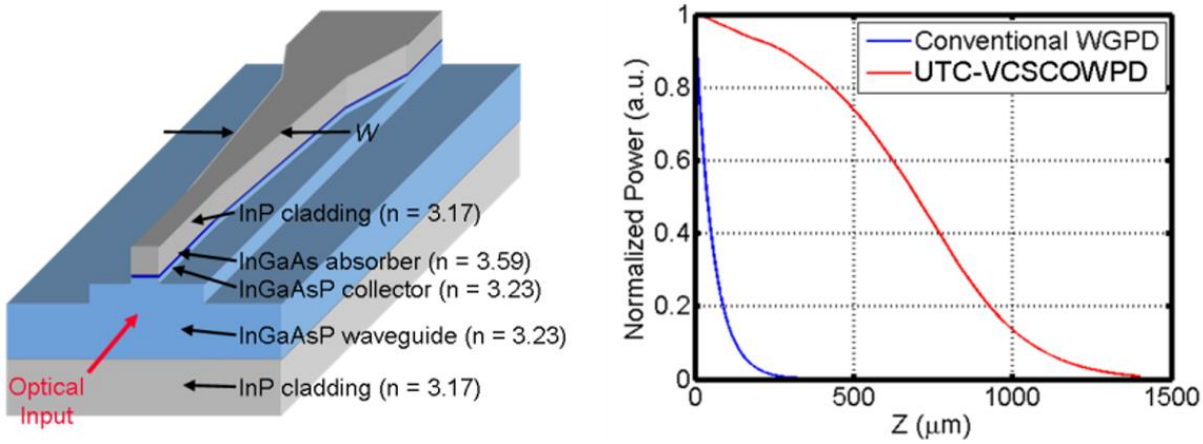

Figure 2-21: (a) Left – Tapered structure of the UTC-VCSCOWPD with 1-μm InP buffer layer, n-doped 5-μm InGaAsP waveguide, 1-μm InGaAsP collector layer, a 50-nm InGaAs absorber, and finally p-type InP cladding with an InGaAs p-type contact layer. (b) Right – simulated, normalized power as a function of device length for a conventional waveguide photodiode with no taper (blue), and a uni-traveling-carrier variable-confinement slab-coupled optical waveguide photodiode (red) [modified from 19].

This work, conducted at MIT Lincoln Laboratory, compared two different taper designs with complementary goals. Increased width along the length of the device increases the optical confinement and subsequently reduces the mode size. Device A was designed with a shorter length (300 μm) and larger input taper (3-6 μm) for high speed and moderate saturation photocurrent, while Device B was designed with a longer length (1.75 mm) and smaller input taper (2-3, 3-6 μm) for moderate speed and high saturation current. Device A achieved a 3-dB bandwidth of 12.6 GHz, responsivity of 0.7 A/W (at 40 mA and -3.5 V bias), and saturation photocurrent of 36 mA. This photocurrent is very high compared to other photodiodes with bandwidths greater than 10 GHz (see Figure 2-22(a) below). Device B achieved a bandwidth of

only 2.5 GHz, but a higher responsivity of 0.8 A/W and saturation photocurrent of over 100 mA (Figure 2-22(b)). At the time in 2011, 100 mA was the highest InP-based WGPD saturation current ever reported. The high performance in responsivity and current-handling can be attributed to the size of the device, which came at the cost of very limited bandwidth.

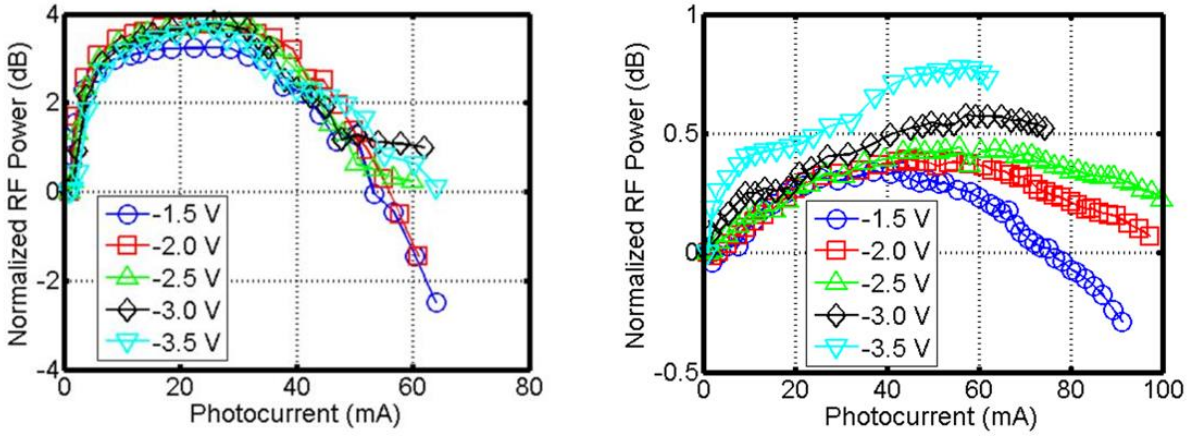

Figure 2-22: (a) Left – Normalized RF power as a function of photocurrent (mA) at varying biases for Device A at 1 GHz, illustrating a 1-dB compression current (current level at which the power degrades by 1 dB from its peak) of 40 mA. (b) Right – Device B projected 1-dB compression current of 150 mA [modified from 19].

The varying device designs of InP-based p-i-n, (M)UTC, and VC-SCOW photodiodes and their corresponding performance found in the literature have informed the design decisions of photodiodes recently fabricated in the Quantum Information and Integrated Nanosystems Group (89) at MIT Lincoln Laboratory.

2.3 MIT Lincoln Laboratory Group 89 Photodiodes

The performance goals of the photodiodes fabricated by Group 89 in this project include a 3-dB bandwidth of 60-100 GHz, responsivity of >0.5 A/W, and saturation photocurrent of 20-100 mA (depending on the photodiode array) for integration into a high-performing microwave photonic system. The device incorporates both MUTC and VC-SCOWPD design to optimize bandwidth, speed, and power handling.

2.3.1 Material structure and design

The material structure and design of the photodiode fabricated by Group 89 is illustrated in Figure 2-23 and 24, below:

Layer Description	Alloy	Target Thickness (nm)	Refractive Index
Contact, p-type	InGaAs	155	3.1680
Cladding, p-type	InP	500	3.1680
Absorber, p-doped	InGaAs	Varied 100-150	
Absorber, undoped	InGaAs	50	
Collector/Matching	InGaAsP	310	3.4100
Waveguide, n-type	InGaAsP	1755	3.2314
Waveguide	InGaAsP	840	3.2314
Semi-insulating InP Substrate	InP	1000	
Oxide insulating layer	SiO2	300	
Pad metal	Gold	500	

Figure 2-23: Epitaxial structure of Group 89's photodiodes with layer description, alloy, target growth thickness in nm, and refractive index.

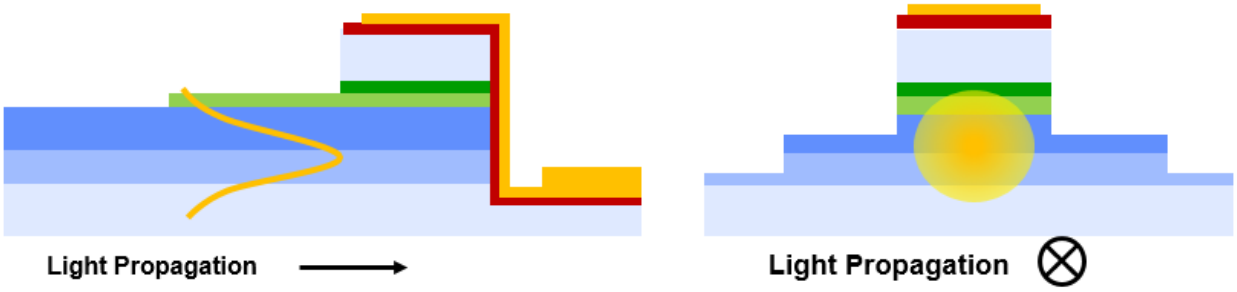

Figure 2-24: (a) Left – Side cross-sectional view of the diode mesa in which the light is propagating from left to right, the mode profile is shown in yellow (not to scale), and with colors corresponding to the layers in Figure 20. (b) Right – Front-end cross-sectional view of the diode mesa in which the light is propagating into the page.

Two different growth designs include a 100-nm and 150-nm p-doped InGaAs absorber. A modified UTC structure was determined to be preferable in bandwidth and saturation characteristics over a p-i-n structure for reasons detailed in section 2.2.6. The novel design aspect of these devices is the use of the matching layer as an optical layer in the mode. Incorporation of the VC-SCOWPD structure was desired for waveguide-coupling and power-handling feasibility, but the size of the device had to be decreased in order to reach the bandwidth performance goals. With smaller devices, tapered layers are more difficult to realize in fabrication. Therefore, the

matching layer is etched as a second tier in the mesa to pull up the mode into the absorber. At the input of the device, the optical mode is approximately 4 μm × 2 μm (see Figure 2-25, below).

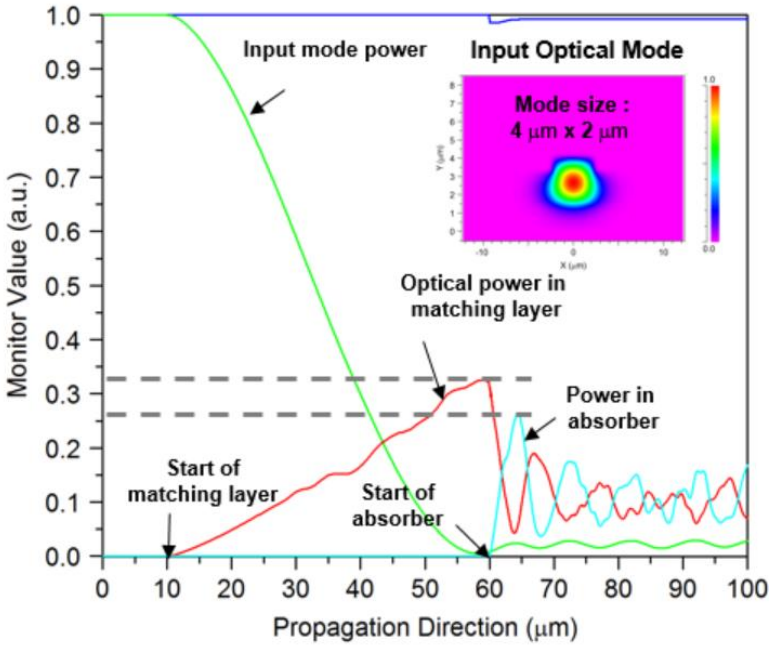

Figure 2-25: Normalized optical power along the length of the device for the matching and absorber layers.

From the model shown in Figure 2-25, the optimal matching layer length was predicted to be 45 μm. This is because the optical power in the matching layer (red curve) steadily increases from the start of the layer until it propagates approximately 45 μm, at which it point it abruptly decreases. The test structures on the wafer include photodiodes with varying matching layer length as well as device size. In one diode array, there are 5 chips with varying matching layer length: 35, 40, 45, or 50 μm. The fifth chip includes matching layers with varying tapered dimensions. Each chip contains 20 photodiodes with varying device lengths: 250, 100, 50, 20, or 10 μm. With the exception of the fifth chip, the widths of the matching layers and devices are 5 μm (see Figure 2-26, below). The fifth chip consists of 10-μm long devices with 45-μm-long matching layers that taper down to varying widths:

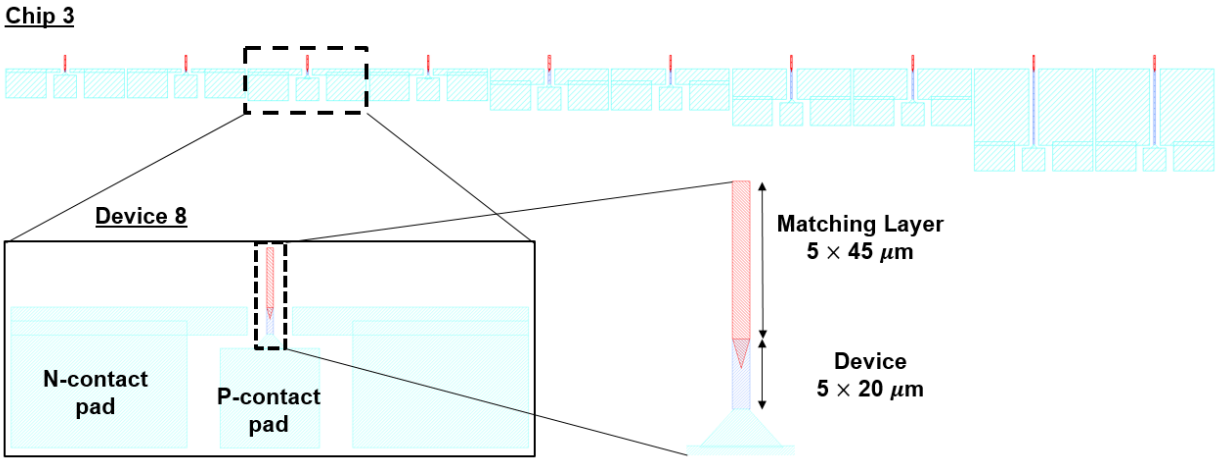

Figure 2-26: KLayout fabrication design of Chip 3 with zoomed-in images of Device 8 and its matching layer (red) and device (royal blue) dimensions. The light blue structures are the ground-signal-ground (GSG) pads for electrical probing. Note: These 10 devices are replicated once for a total of 20 devices on each chip.

2.3.2 Fabrication

The fabrication process for these InP-based photodiodes involve a four-tier, self-aligned mask/etch process. The photodiode active area (the absorber) is the first etch, followed by the matching layer, input waveguide, and finally the electrical isolation region. The scanning electron-beam micrograph (SEM) shown in Figure 2-27 demonstrates successful alignment of the devices on the InP substrate, often a challenging process in photodiode fabrication. Next, p-type ohmic metal was deposited, the devices were passivated, and then p-type ohmic metal was deposited. The deposition of the pad metals was found to be the greatest challenge in the fabrication process for these devices; the metal had to cover the p-type contact of absorber and step down the back of the device to the signal pad. Figure 2-28 illustrates successful deposition and coverage of the pad metals.

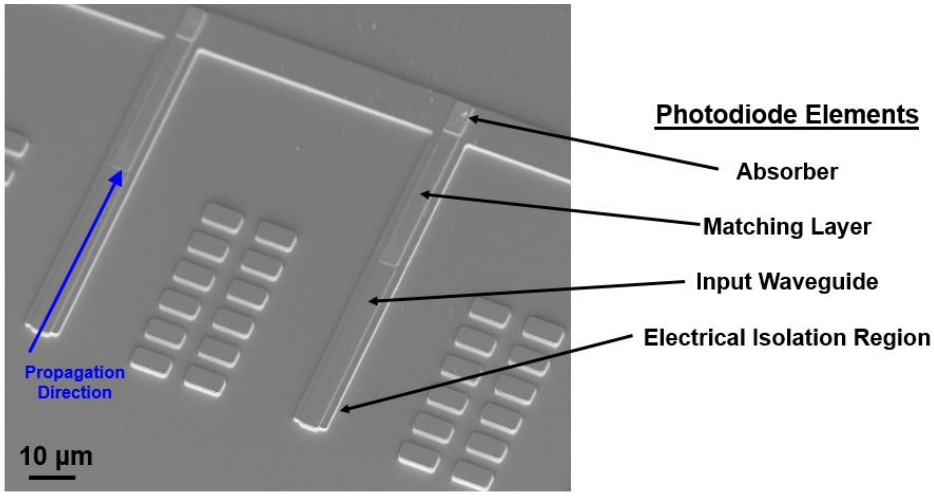

Figure 2-27: Scanning electron-beam micrograph (SEM) image of the four-tier design of the photodiode devices including the absorber (active region of the device), matching layer, waveguide, and the electrical isolation region.

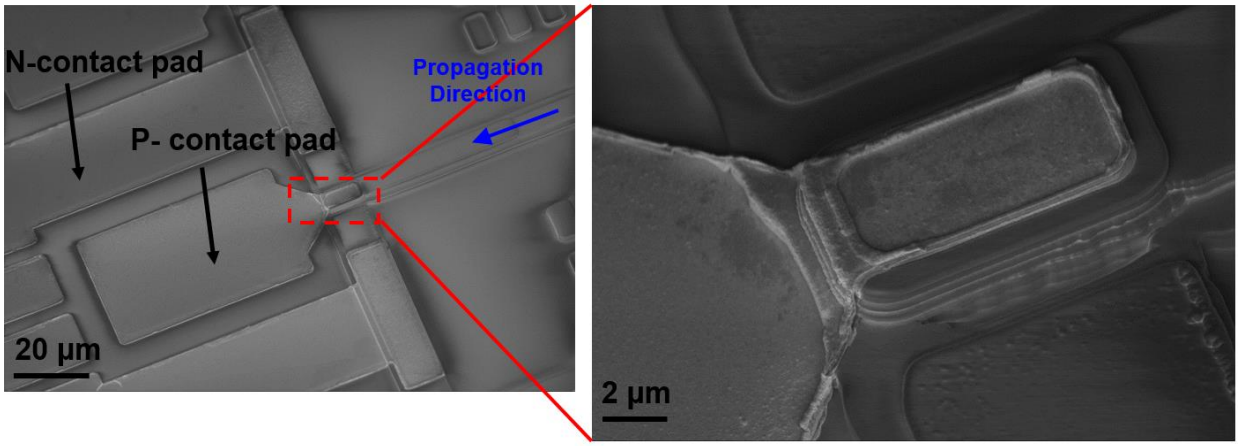

Figure 2-28: Scanning electron-beam micrograph (SEM) images of the metal contact pads deposited during fabrication.

2.3.3 Initial testing

Following the fabrication of these photodiodes, the individual chips were cleaved and mounted onto copper submounts for testing. Initial testing showed negligible dark currents in the nano-ampere (nA) range, a breakdown voltage greater than -5 V, and good uniformity across the chip. Initial measurements of the 45-μm matching layer, 10-μm device (total area 50 μm^2) yielded an external responsivity of ~0.35 A/W (without AR-coating) at 0.3 mA and biased at -3 V. The 250-μm device reached responsivities up to 0.57 A/W, also without AR-coating (see Figure 2-29, below).

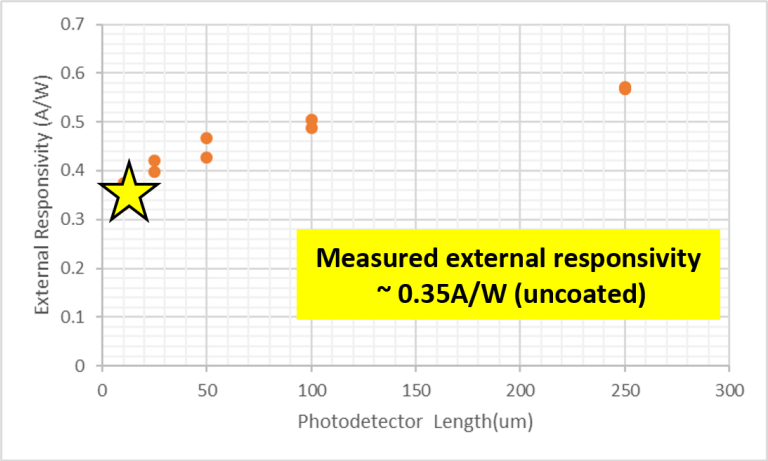

Figure 2-29: Initial responsivity measurements of the 45-μm matching layer devices as a function of device length. The responsivity was measured at 0.3 mA and biased at -3 V.

2.3.4 RF Limitations

During initial RF testing of the first generation devices, the RF loss measured from the test structures was much higher than expected. It was discovered that there was an error in an etching step that resulted in an unintentionally-doped InP buffer layer between the substrate and the pad. The doped region creates capacitance in the substrate that severely limits the RF performance of the devices. The etch depth will be corrected in the second-generation devices, and for this reason the RF performance of the first-generation devices will not be a focus of this project.

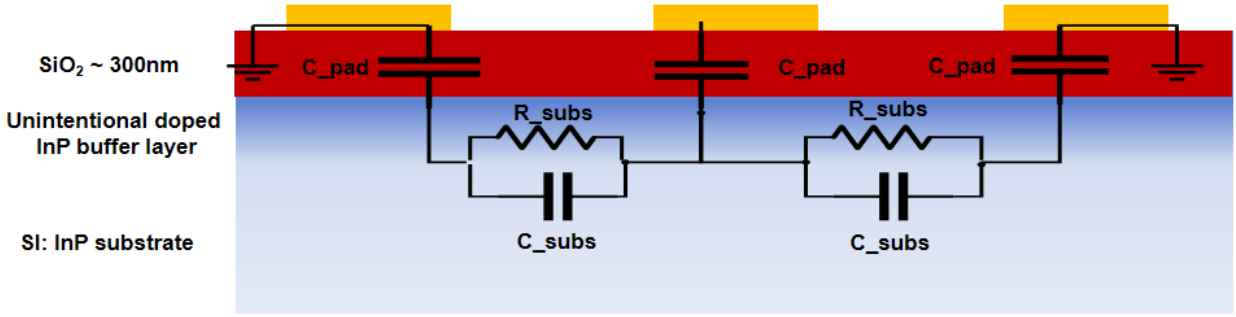

Figure 2-30: A schematic diagram of the unintentional RF coupling to the InP substrate found in Group 89's first-generation devices.

3. Methodology

In order to accomplish the project goal of fully characterizing waveguide-integrated MUTC VC-SCOWPDs in the effort to further understand mechanisms of high-performing devices for MWPIC integration, the project includes the following objectives:

1. Understand relevant device physics concepts such as Maxwell's equations, optical properties of semiconductor materials, and electron/hole transport in III-V hetero-structures, as well as how these concepts will manifest in device testing
2. Perform device tests to characterize the following parameters of the fabricated photodiodes: IV curves and dark currents, optical external responsivity, and saturation photocurrent
3. Develop a theoretical model for optical propagation through the fabricated material structure to compare with measured results and eventually inform future design recommendations.

3.1 Objective 1: Understand and correlate device physics concepts

To accomplish the first objective, the study conducted an extensive literature review to summarize the current state of photodiodes for high frequency applications. This involved comparing the performance of different types of fabricated photodiodes and correlating measured characteristics with specific aspects of the device design. Ranges of values for the different performance metrics were assigned to three categories: poor, moderate, and high performing. The resultant summary of the literature review served as a rubric for the results measured in the second objective.

3.2 Objective 2: Perform device tests

For the second objective, the device tests were performed in the Integrated Photonics Lab, room D-227, modifying pre-existing bench set-ups for DC measurements. Carrying out these tests involved developing a custom LabVIEW program that automatically steps through different variables such as wavelength or voltage to acquire a complete data set. Analysis of the measurements were completed with scripts developed in MATLAB.

3.2.1 DC test setup

Direct current (DC) measurements for photodiodes include dark current, IV (current-voltage) response, and external responsivity. To measure dark current, the Keithley instrument sources voltage and measures current when the fiber laser is not emitting light. Since photodiodes operate under reverse bias, a typical voltage range to measure is -5 V to -0.5 V. In general, dark current values should remain under 10 μA for the leakage in the device to be considered negligible. Recording the IV response of the device also indicates whether the photodiode is functioning with ideal exponential behavior, if the device has shorted (linear IV response), or if the device fused open (no current). The current at which the device fails (shorts/fuses) is also a notable measurement. To make electrical contact with the device, a three-pronged GSG probe lands on the photodiode's metal GSG pads.

To measure external responsivity, an Agilent laser sources light at a chosen wavelength to the Erbium-doped fiber amplifier (EDFA) to provide an increased power range. The amplified light then returns to the Agilent mainframe into its variable optical attenuator (VOA) to control the amount the power is attenuated, or weakened. Next, the attenuated optical signal is sent into a splitter where 99% of the light is directed out of the fiber to the photodiode chip, and the other 1% is measured by an ILX Lightwave multimeter to provide a constant power reading. The ratio between the two feeds yields the amount of loss present in the 1% tap, and the power at the chip at any time can be calculated by adding this loss to the tap reading. For this setup around 1550 nm, the tap loss is approximately 14.3 dBm. As an example, if the multimeter was reading -17.3 dBm, the power at the photodiode would be approximately -3 dBm. This conversion can be considered constant across the small wavelength range of 20 nm.

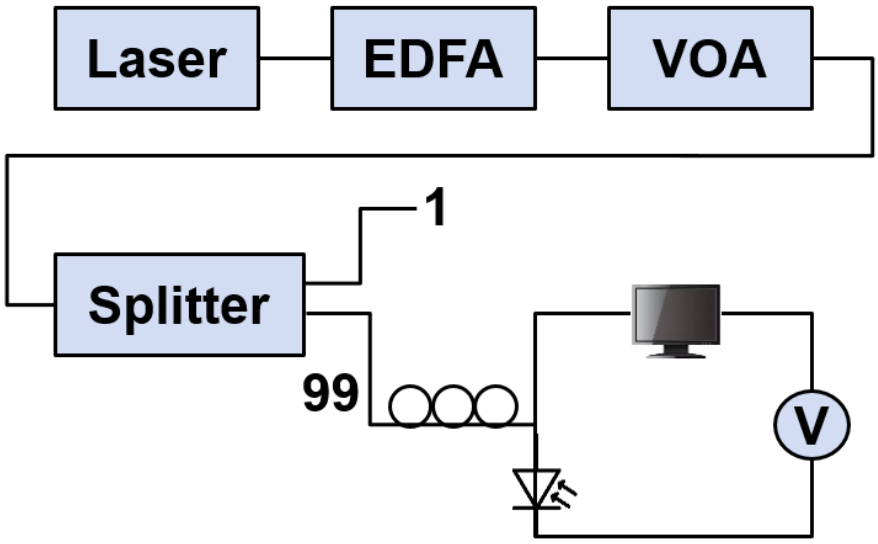

Figure 3-1: Setup for direct current (DC) measurements in the Integrated Photonics Lab. EDFA represents the Erbium-doped fiber amplifier, and VOA represents the variable optical attenuator.

Measuring the responsivity of the device involves making electrical contact with the probes on the metal pads and coupling the optical fiber into the waveguide of the device. The fiber is mounted on a three-axis stage, and piezo-electric actuators allow for ultra-fine stage control and coupling. When optimizing the fiber coupling, the wavelength of the light source is set to 1550 nm and the device is biased at -3 V. The photodiode chip and copper sub-mount sit on a heatsink that enables steady control of the temperature of the device (see Figure 3-2, below).

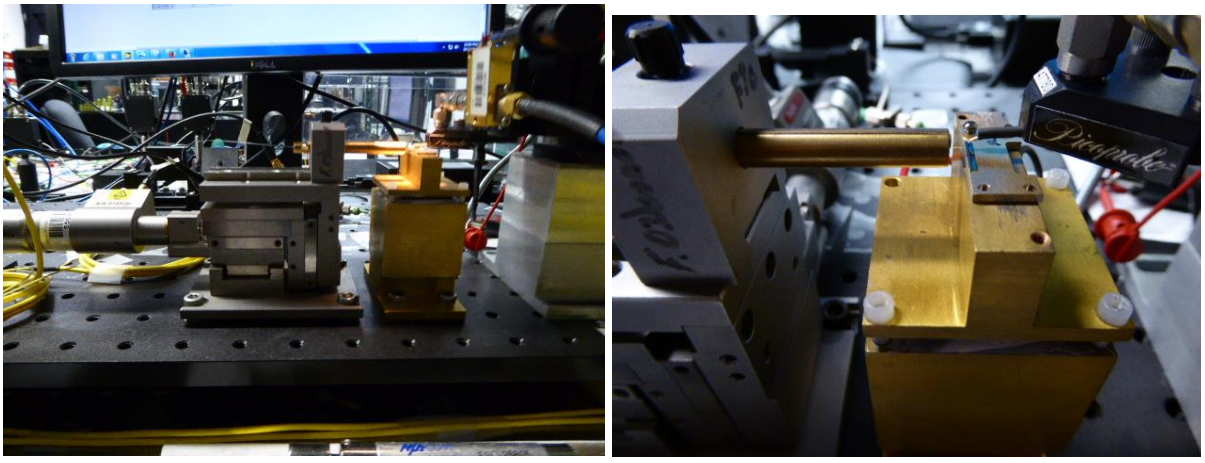

Figure 3-2: The optical fiber (enclosed in bronze cylinder, not visible) mounted on the three-axis stage controlled by piezo-electric actuators (left). The fiber coupled into the mounted chip and electrical probes (right).

3.2.2 Data collection

To automate the data collection process, a custom LabVIEW program allows the user to step through different voltages, attenuation levels, and sweep through a wavelength range while measuring photocurrent and tap power at every point (see Figure 3-3, below). Although the LabVIEW program can automatically step through the different bias voltages, it is important to monitor the fiber coupling throughout the sweep to check for drifting from the optimal position. The primary yield of this data collection was responsivity as a function of wavelength, input power, and bias voltage for different device lengths, matching layer lengths, and absorber thicknesses.

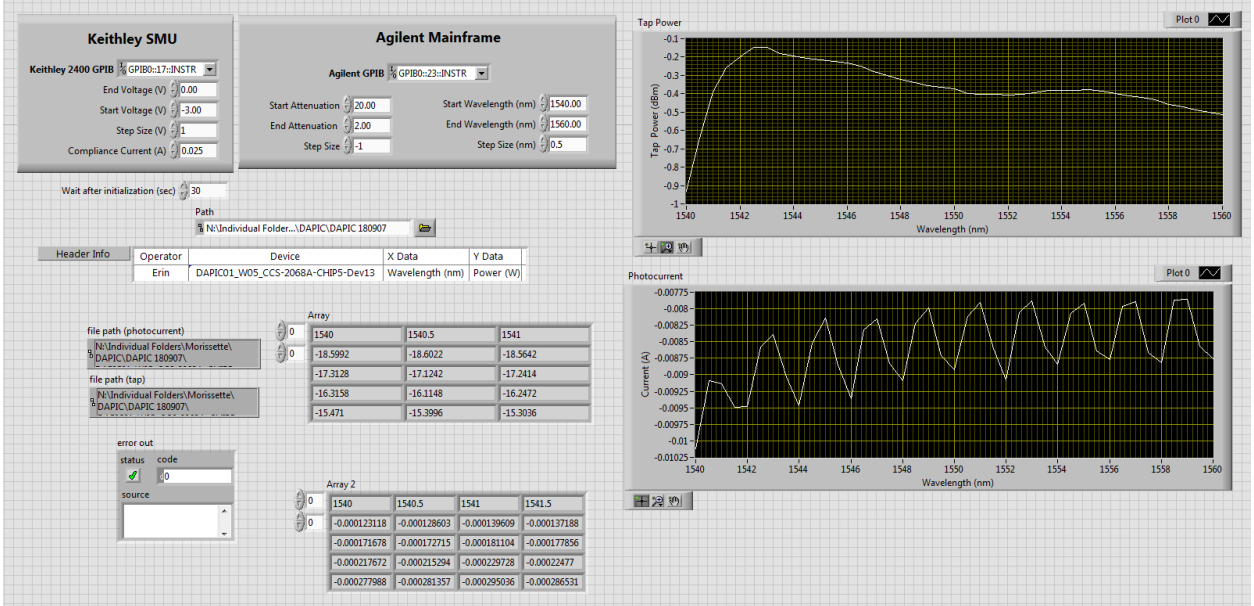

Figure 3-3: Front panel of the LabVIEW program developed to automate data collection for each device (Note: higher attenuation values decrease the optical input power).

3.3 Objective 3: Develop model for optical propagation

For the third objective, the study will include optical propagation modeling executed in MATLAB utilizing a derivation from resonance in a ring. Together, these objectives will allow the investigation to exhaustively compare theoretical performance according to device physics,

past device performance reported in the literature, and measured performance from Group 89's UTC-PDs. This methodology is summarized in Figure 3-4 below:

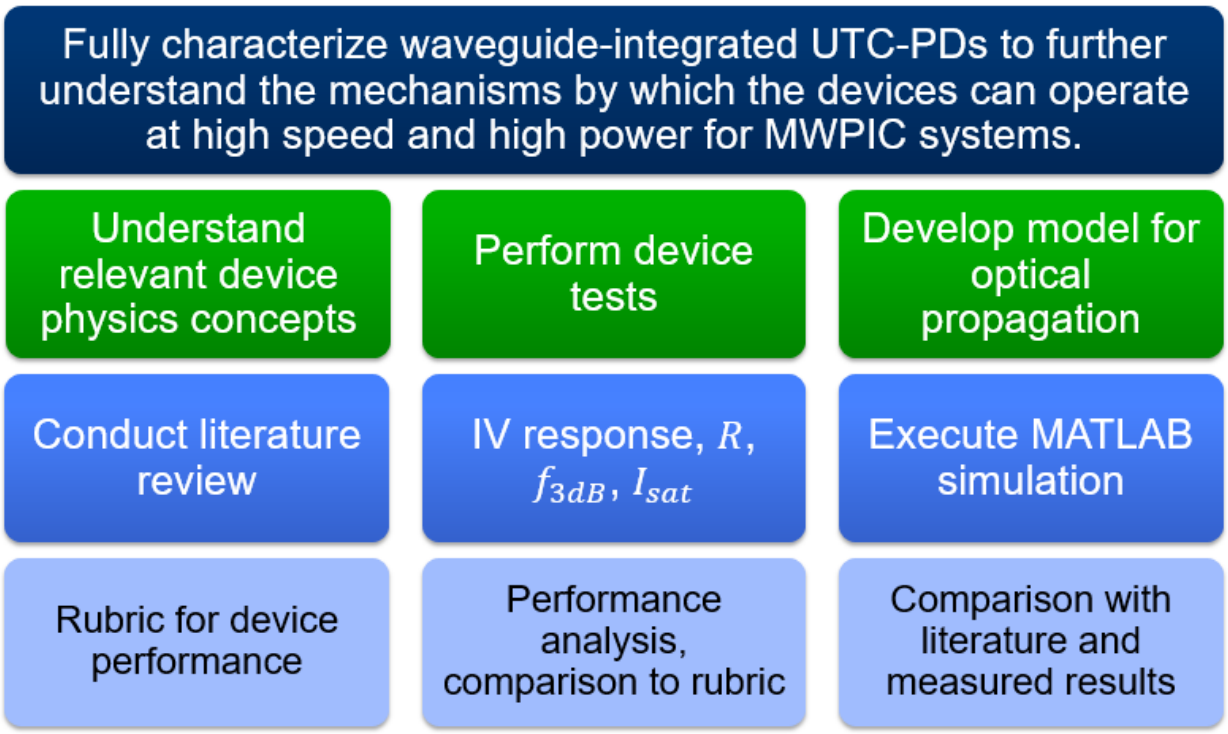

Figure 3-4: Methodology flow chart in which dark blue represents the goal, green the objectives, royal blue the specific tasks, and light blue the deliverable.

3.4 Timeline

	Week 1	**2**	**3**	**4**	**5**	**6**	**7**	**8**	**9**
Literature Review									
Simulation Familiarization									
Data Collection									
Simulation and Analysis									
Writing/Presentation Prep									

Table 3-1: Proposed timeline for the project across the 9-week term.

The first week of the project consisted of a literature review of existing photodiode technology and their device designs. The second week marked the beginning of data collection

with simultaneous exploration/familiarization of necessary MATLAB scripts and derivations. These tasks continued into the third week while some initial data analysis was performed. From Week 3 to 8, the study involved intensive data collection, analysis, and modeling. Lastly, Weeks 8 and 9 were dedicated to final data collection, full-draft editing, and presentation preparation.

4. Results and Discussion

This chapter will present the results from each objective detailed in the methodology. These results include a summary of the literature review, DC measurements of the devices, and outcomes of modeling done in MATLAB.

4.1 Current State of the Technology

The performance metrics and corresponding designs of photodiodes detailed in the literature were summarized and compared. Highlights from this summary are shown in Table 4-1, below. These devices were chosen because the photodiodes design in Group 89 incorporated design elements from all three, aiming to optimize speed, efficiency, and current-handling. This summary also further illustrates the trade-offs present in current photodiodes. The UTC photodiode had a very high bandwidth of 170 GHz due to a small device area, but as a result the responsivity and current performance suffered. Contrarily, the variable-confinement slab-coupled optical waveguide photodiode (VCSCOWPD) had a superior saturation photocurrent of over 100 mA due to its very large device area, so the bandwidth suffered.

Metric	Device 1, CPW UTC[1], Rouvalis 2012	Device 2, p-i-n, Achouche 2006	Device 3, UTC VCSCOWPD[2] Klamkin 2011
3-dB bandwidth, f_{3dB}	170 GHz (Area = 20 μm^2)	47 GHz (125 μm^2)	2.5 GHz (~5500 μm^2)
Responsivity, R	0.27 A/W	0.81 A/W	0.8 A/W
Saturation photocurrent, I_{sat}	-5 dBm at 170 GHz	11 mA	> 100 mA

Table 4-1: Highlighted devices from the literature and their performance in 3-dB bandwidth, responsivity, and saturation photocurrent. Data highlighted in green signify the performance metric that was emphasized in the work and the design.

The complete summary of photodiode in the literature are shown in Figure 4-1 below.

Author	Year	Description	3-dB BW (GHz)	Responsivity (A/W)	RF output power (dBm)	Isat (mA)	(Frequency) (GHz)	Dimensions (um)	Area (um^2)	Other	AR?
Achouche	2004	ECW UTC	50	0.76		22	50	4x15	60	Responsivity with almost no bias depedence, misalignment tolerances 5 (H) and 2 (V)	yes
Achouche	2006	p-i-n	47	0.81		11	40	5x25	125	Alignment tolerance 2.7 (V)	yes
Beling	2013	MUTC (on SOI)	15	0.26				?x100		no AR coating	no
			24	0.25				?x50			
			30	0.11				?x25			
		2-element array	15	0.2	9.3	42	20	10x37	370, total 740	Record high 630 mA GHz	
		4-element array	8		10.2		20	10x20	200, total 800		
Q. Li	2017	E WG integrated MUTC	105	0.1	-4.8		105		24	Very similar to Group 89 devices	
			92	0.15	2, 1.3		100, 105		50		
Rouvalis	2012	ECW UTC	90	0.35	1		110	3x15	45	No AR coating	no
Rouvalis	2012	CPW-integrated UTC	170	0.27	-5, -9		170, 200		20		
Rouvalis	2012	TW UTC	108	0.53				3x25	75		
Bach	2004	WG p-i-n	100	0.66	-9	22	100	5x20			
Klamkin	2011	UTC VCSCOWPD	12.6	0.7		34	10	3-6x300			
			2.5	0.8		> 100	1	2-6x1750			
		Key:	>60	>0.5		>40					
			<30	≤.2		<20					

Figure 4-1: The complete literature performance review of various InGaAs/InP photodiodes with various designs.

4.2 Photodiode Characterization

The modified uni-traveling carrier photodiodes fabricated by Group 89 were characterized by the methods described in section 3.2. These tests yielded measurements of dark current, failure current, and responsivity as functions of wavelength and power. Performing the measurements on photodiodes with different material and structure designs allowed for the comparison between absorber layer thickness, matching layer length, and device length.

4.2.1 Dark current

To test the initial functionality and leakage of the photodiode, the IV response of each photodiode was measured without input optical power. An example of a dark current voltage sweep is shown in Figure 4-2, below. The device begins to break down at -5 V, and exhibits exponential behavior with positive voltage. The average current between the breakdown and exponential increase is 4.7×10^{-8} A, or 47 nA. Confirming that the dark current is not a significant fraction of the photodiode current implied that any leakage current in the device can be considered negligible compared to the photocurrent in the mA range.

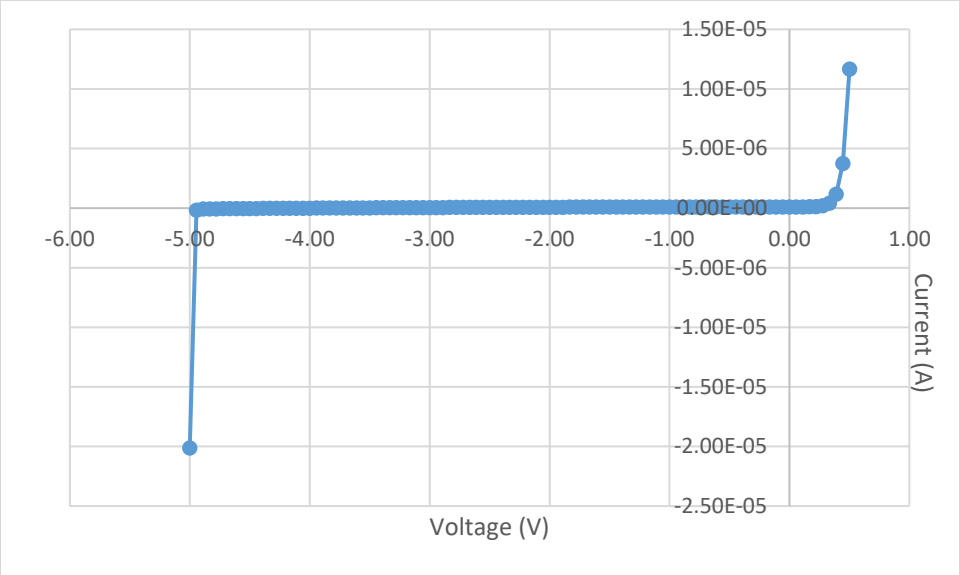

Figure 4-2: An example of the IV response of a 25-μm^2 device.

4.2.2 Device current handling

In order to quantify the current handling of the devices, photodetectors of various sizes were tested to failure. The failure current was found to be a function of device size. While the smaller devices will yield the highest 3-dB bandwidth and fastest performance, higher current densities result in decreases current handling performance. Therefore, the current handling of the smallest devices is of the greatest interest. In Figure 4-3, below, the failure current is plotted as a function of the log of device area, ranging from 25 μm^2 to 1250 μm^2. Generally, the failure current increases with device area. Most significantly, even the devices with the smallest area (and highest projected bandwidth) fail at currents greater than 8 mA, which is reasonable for system performance.

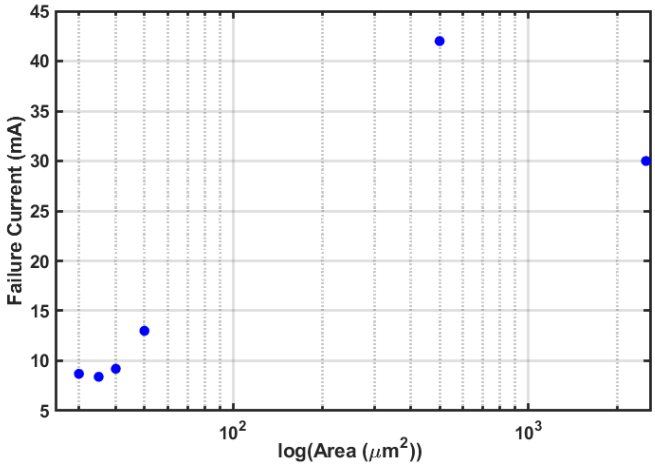

Figure 4-3: A semi-log plot of failure current and device area.

4.2.3 Failure mechanism

More surprisingly, it was discovered that the mechanism of failure also depends on the device size. When the smaller diodes (10-μm length) hit the point of failure, the current measurement abruptly drops to zero (see Figure 4-4, below). They also present with burn marks at the absorber exactly at the moment of failure (see Figure 4-5, below). This implies that the device fuses open at the location where current density is expected to be the greatest.

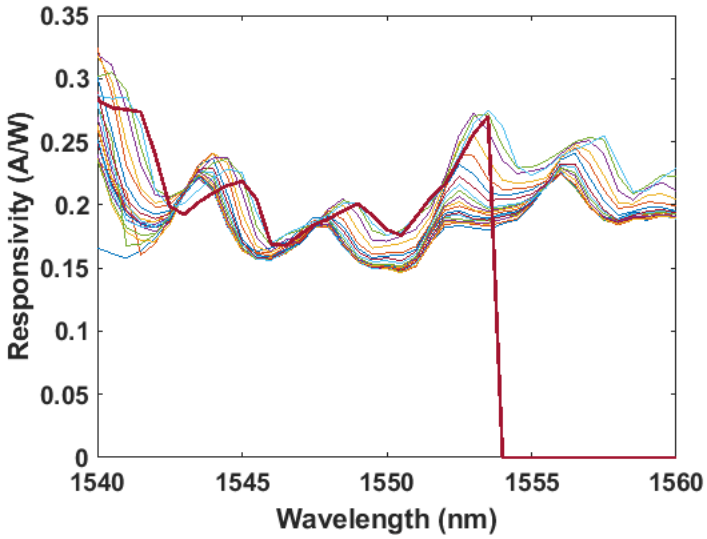

Figure 4-4: Plot of responsivity as a function of wavelength for a 10-μm-long device where each curve is a different power level. The fuse is shown by the red curve in which the current (and subsequently the reponsivity) drops to zero.

Figure 4-5: A 10-μm device before (left) and after (right) failure, with burn marks on the absorber visible in the red box.

However, the larger devices did not seem to possess the same failure mechanism. For example, when the 250-μm device failed, the current increased in a manner consistent with a shorted circuit (see Figure 4-6, below). There were no burn marks visible on the absorber, but there appeared to be marks on the ground pads. A similar result was observed in initial testing prior to the project. This would imply that the device is shorting in an area where the current density is not expected to be significant. Therefore, the failure mechanism of the photodetectors is not consistent across varying devices, and additional testing is required to precisely describe the location of the failure (see Chapter 5).

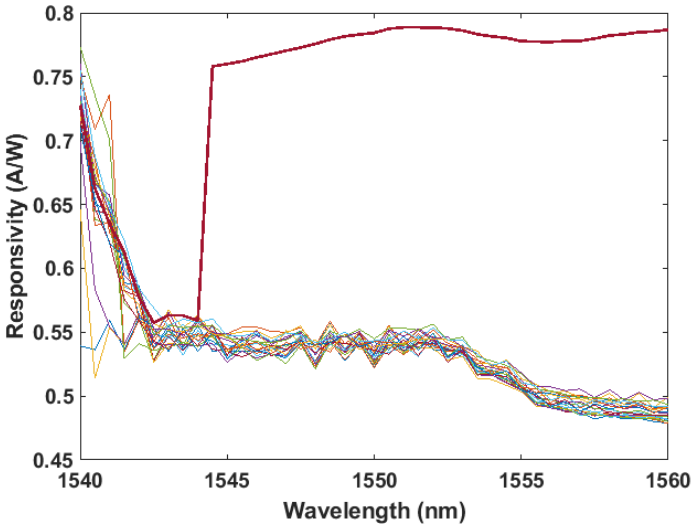

Figure 4-6: Responsivity as a function of wavelength for a 250-μm-long device. The device shorting is shown by the red curve in which the current and responsivity increase.

4.2.3 Responsivity as a function of matching layer length, device length

The photodiodes were fabricated with device lengths ranging from 10 to 250 microns and matching layer lengths from 30 to 50 microns. In general, external responsivity increases as device length and active area increases (See Figure 4-7, below). The 45-μm matching layer devices ranged from a responsivity of 0.31 A/W for the 10-μm-long device to 0.57 A/W for the 250-μm-long device. The lower, outlying responsivities of the 250-μm, 35-μm matching layer photodiodes are expected to be a result of damage during cleaving. Regarding matching layer length, the 45-μm matching layer devices appear to perform better than the 35 and 50-μm matching layers. This data supports the prediction from modeling that the optimal matching layer length would be 45 μm (see Section 2.3.1). The improvement is particularly evident with the smaller devices (10 and 25-μm) that have the greatest projected bandwidth and are the most likely candidates for system integration.

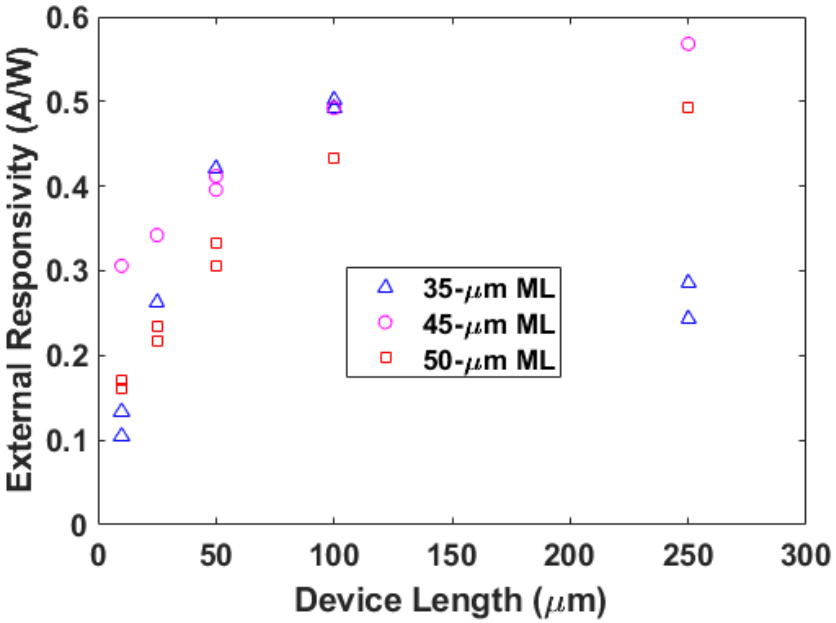

Figure 4-7: External responsivity (A/W) as a function of device length (all device active areas shown have a width of 5 μm) as well as matching layer (ML) length.

4.2.4 Responsivity as a function of wavelength, power

Initially, the most notable features of the responsivity plots were distinct oscillations with changes in wavelength. Although the oscillations first appeared to resemble trends found in literature Zhou *et al.* [5], the frequency of the measured sinusoidal signal is not the same for comparable devices (see Figure 4-8, below): the measured period is approximately 4 nm, while the period in the literature is 10 nm. The cause of the oscillations is not mentioned in [5]. To determine the mechanism of the higher frequency oscillations in Group 89's photodiodes, various Fabry-Perot cavities (also referred to as etalons) in the fiber-device system were investigated. Light reflecting back and forth in these cavities result in destructive and constructive interference, which can manifest as oscillations in responsivity with changing wavelength.

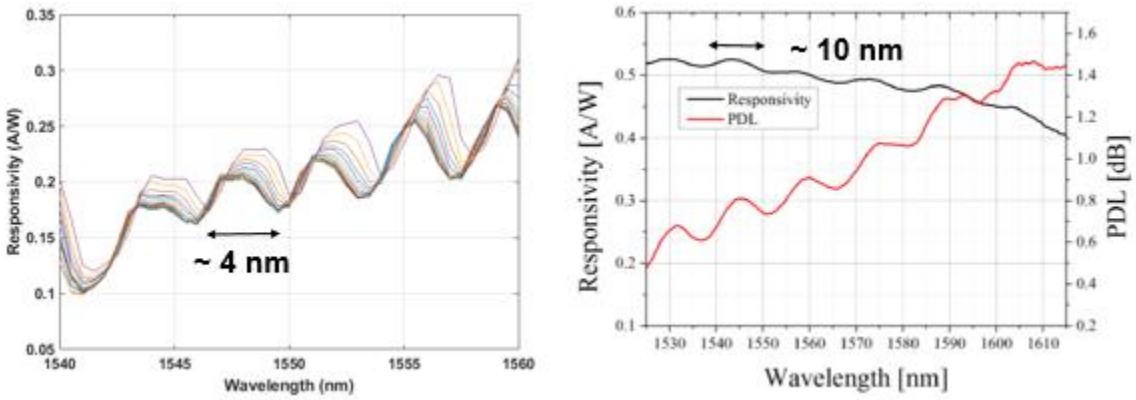

Figure 4-8: Measured responsivity as a function of wavelength for a uni-traveling carrier (UTC) photodiode (left), and the responsivity (black line) of a UTC photodiode from Zhou *et al.* [5] (right).

The first etalon investigated was the air cavity between the end of the optical fiber and the edge of the device. If the oscillations were caused by these two reflective surfaces, shifting the fiber in the z-direction (the optical axis, see Figure 4-9 below) would change length of the cavity and subsequently the frequency of the oscillations. However, moving the fiber away from its optimized position only decreased the responsivity and did not alter the frequency (see Figure 4-10, below). Therefore, the etalon between the fiber and edge of the device was ruled out as the cause for the responsivity oscillations.

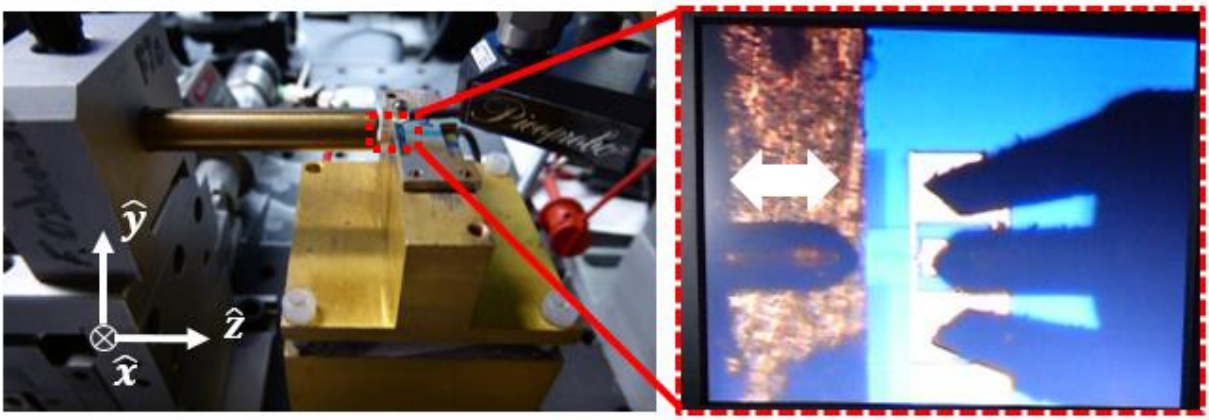

Figure 4-9: (Insert) The optical fiber up against a 25-μm device, and the cavity of air between them (not visible).

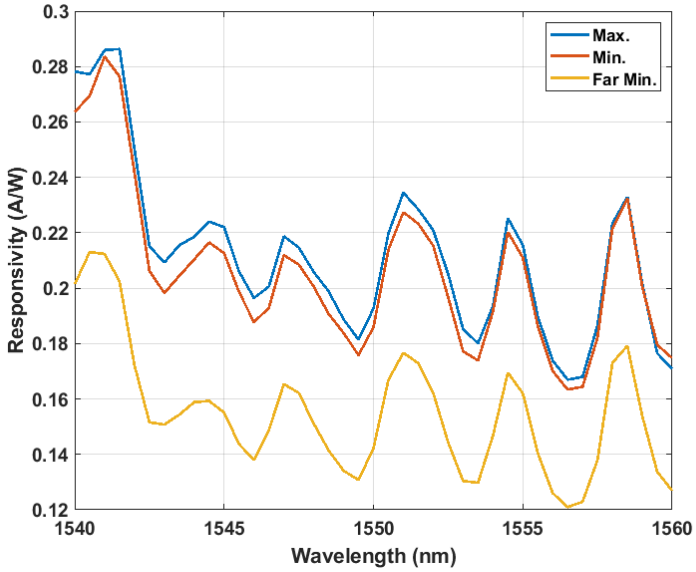

Figure 4-10: Responsivity as a function of wavelength for a 25-μm photodiode. The curves correspond with optimized fiber coupling position (blue), a local minimum further away along the optical axis (red), and a minimum even further away from the edge of the device (yellow).

Upon further inspection of the response for varying-sized photodiodes, it was discovered that the frequency of oscillation appeared to depend on the length of the device. Direct comparison revealed that increased length resulted in an increased frequency of fluctuations in the responsivity as a function of wavelength, and vice versa (see Figure 4-11, below). This suggested that the cavity responsible for the oscillations included the active area of the

photodiode, the component of varying length. To investigate this possibility, the length of a cavity with a corresponding free spectral range of 1.5 – 5 nm (the approximate period of the responsivity oscillations) was calculated:

$$\Delta\lambda_{FSR} = \frac{\lambda^2}{n_g L} \rightarrow L = \frac{\lambda^2}{n_g \Delta\lambda_{FSR}} \tag{4-1}$$

where λ = 1.55 μm, $\Delta\lambda_{FSR}$ ~ 1.5 – 5 nm, and the group index of the photodiode, $n_g = n/(1 + \frac{n}{\lambda}\frac{dn}{d\lambda}) \approx 4.2248$. This range of free spectral wavelength values yields cavity lengths from 380 – 110 μm. These lengths roughly correspond to the devices shown (total lengths 325 – 85 μm) in Figure 4-10 with their respective oscillation periods. Since the group index of the device and its dependence on wavelength is not explicitly known, the difference in lengths can be attributed to this approximation.

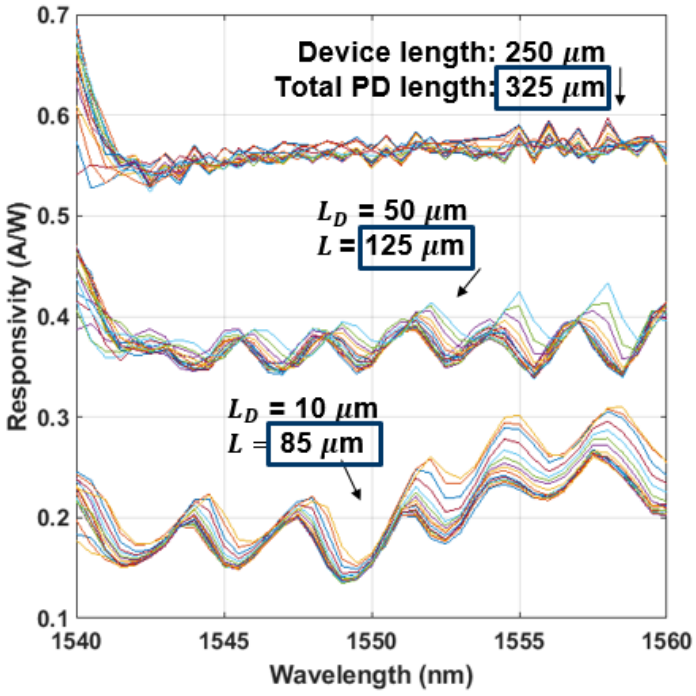

Figure 4-11: The responsivity as a function of wavelength for a 250-μm, 50-μm, and 10-μm device (L_D). The total length, L, includes the matching layer and waveguide length as well as the absorber length. Increasing device length is shown to increase the frequency of oscillation.

The initial correlation in free spectral range and cavity length indicated that the device itself was acting as an etalon, and modeling was necessary to provide further evidence of the mechanism.

4.3 Device Modeling Results

In attempting to describe the mechanism of oscillation in the photodiode responsivity as a function of wavelength, theoretical modeling of the suspected etalon (or Fabry-Perot cavity) could be compared to measured data. Given the time constraint, modeling using Lumerical fell out of the intended scope of this project, but MATLAB modeling was sufficient in describing the theoretical behavior of reflections in the photodiode.

4.3.1 Matlab reflection modeling

To model the responsivity and normalized transmission as a function of wavelength in a reflective cavity, the derivation for resonance in a ring was utilized. The maximum responsivity was first calculated about the center wavelength:

$$R_{max} = \frac{q}{hc} \cdot \lambda_R \tag{4-2}$$

which is simply the ratio of one generated electron per input photon. Next, the loss in the cavity due to the difference in measured and maximum responsivity was calculated in dB:

$$\alpha_{dB} = \frac{\log_{10}(10^{10\log_{10}\left(\frac{1-R}{R_{max}}\right)}/10)}{L_d} \tag{4-3}$$

where L_d is the length of the device. Additionally, the Fresnel reflection was calculated:

$$R_f = \frac{(n-1)^2}{(n+1)^2} \tag{4-4}$$

in which n is the index of refraction of the mode in the photodiode, assumed to reflect compared to air. The reflection is used to describe the field coupling coefficient of the mode, κ, and since the device is symmetric, $\kappa_B = \kappa_D = \sqrt{R_f}$. To convert α_{dB} into units of inverse length, $\alpha = 0.5\log(10^{\alpha_{dB}/10})$. Lastly, the phase was calculated as the following:

$$\phi = i\left[\frac{2\pi f_0}{cnL} + \frac{n_g}{c}2\pi L_d(f - f_0)\right] + \alpha 2L_d \tag{4-5}$$

in which i is the imaginary number, c is the speed of light, f_0 is the center frequency, and n_g is the group index of the device (described in section 4.2.4). Therefore, the transmission is as follows:

$$A_{out} = \frac{\sqrt{1-\kappa_B^2} - \kappa_B^2\sqrt{1-\kappa_D^2}}{-\sqrt{1-\kappa_B^2}\sqrt{1-\kappa_D^2} + e^{\phi}} \tag{4-6}$$

which due to symmetry can be simplified to

$$A_{out} = \frac{(1-R_f)^{3/2}}{-(1-R_f) + e^{\phi}} \tag{4-7}$$

The normalized transmission, $|A_{out}|^2$, as a function of wavelength for a given device length and corresponding responsivity yields the following graph is shown in Figure 4-12, below.

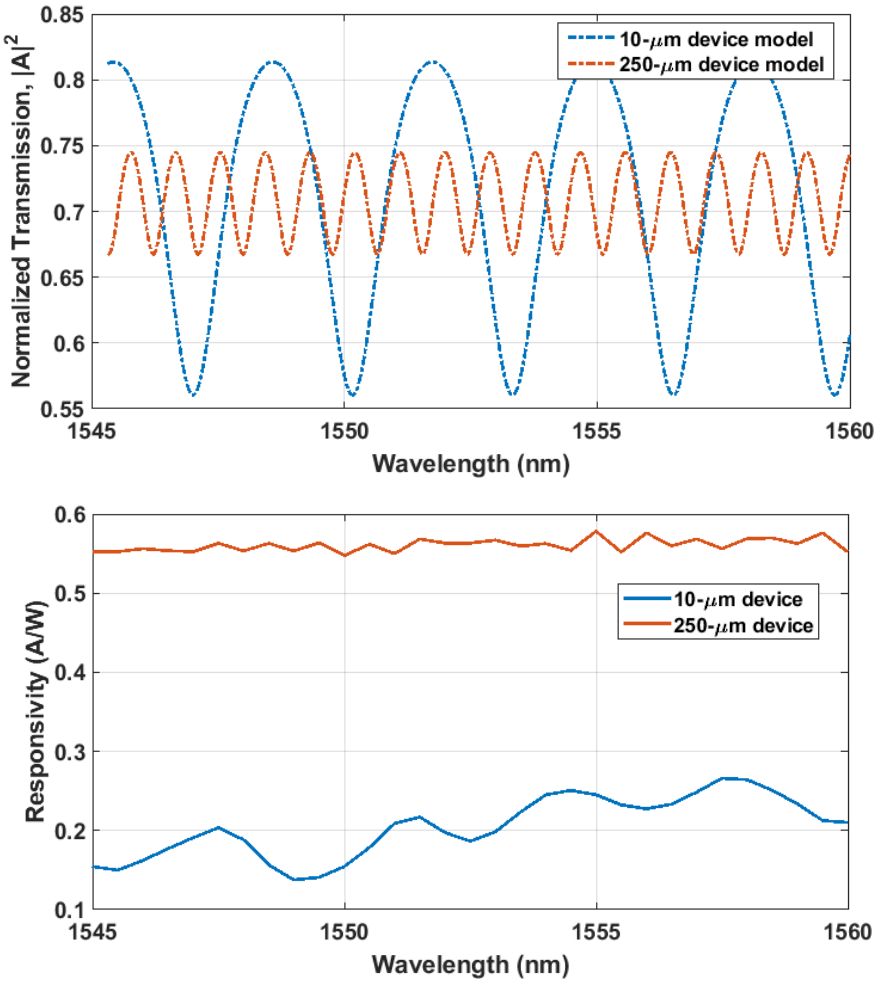

Figure 4-12: Top - Results of modeling normalized transmission as a function of wavelength for the shortest and longest devices, 10-μm and 250-μm respectively. Bottom – measured responsivity as a function of wavelength for the same devices.

In comparing the modeled transmission with measured responsivity of the two different length devices, it is evident that the amplitude as well as the period of the oscillations correspond. The values of transmission and responsivity on the y-axis should not be directly compared, but transmission in the cavity impacts the modes pulled up into the active area measured as photocurrent and responsivity. The decreased fluctuations in the transmission of the 250-μm device results in the increased responsivity of approximately 0.55 A/W. Contrarily, the larger fluctuation in transmission for the 10-μm device manifests as a lower responsivity of ~0.2-A/W. Both the modeled and measured oscillation periods for the 10-μm device is ~4 nm, and for the 250-μm device 1 nm. Since the model and the measured data are consistent, the mechanism of the oscillation can be confidently described as a result of reflection in the whole device.

4.3.2 Anti-reflective coating

To definitely confirm the mechanism for the smaller-scale oscillations as reflection, the final step was to apply an anti-reflective (AR) coating to the devices, repeat responsivity measurements, and compare the same devices before and after. The AR-coating was applied to the back of the photodiode where the pad metals are believed to act as a mirror (see Figure 4-13, below). Ti_3O_5 and SiO_2 were chosen as the AR-coating layers with thicknesses that result in destructive wave interference. Figure 4-14 compares the responsivity as function of wavelength for the 2.5 × 10 μm device with and without AR-coating. It is clear that the AR-coating eliminates the higher-frequency oscillations as well as increases the overall responsivity.

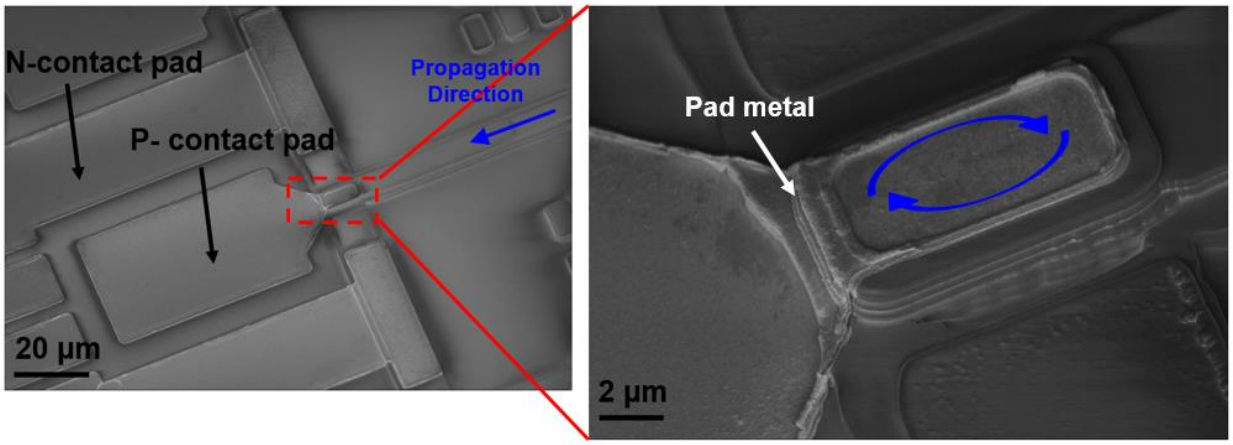

Figure 4-13: A scanning electron micrograph (SEM) of the photodiode, with the insert highlighting the pad metal over the back of the device.

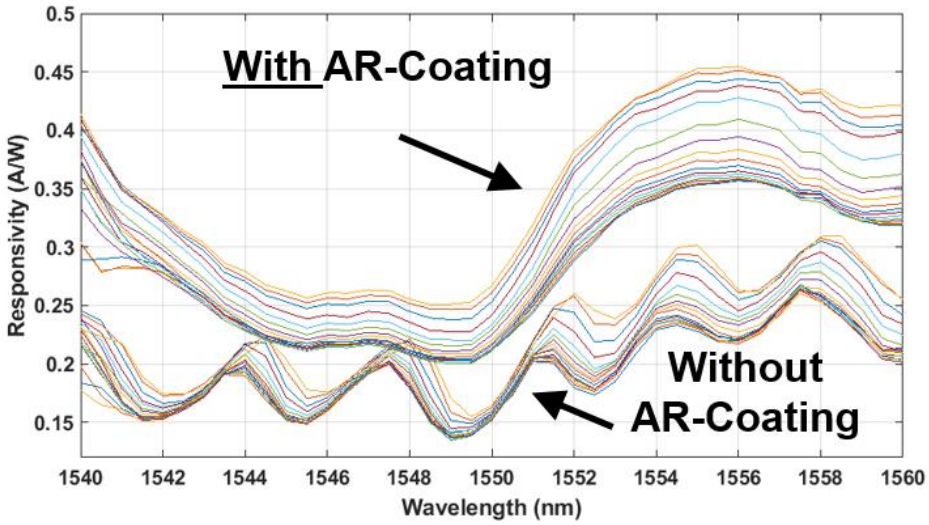

Figure 4-14: Responsivity as function of wavelength for the 2.5 × 10 μm device with and without AR-coating.

While a larger, overlying oscillation still remains in the AR-coated devices, the period of this oscillation is on the order of 10 nm which is comparable to the literature examples. Similar results were obtained for devices of all sizes. Therefore, it can be confirmed that the reflections in the photodiode were the mechanism of the higher-frequency oscillations. Additionally, Figure 4-15 shows the responsivity as functions of device length and matching layer length including the AR-coated devices:

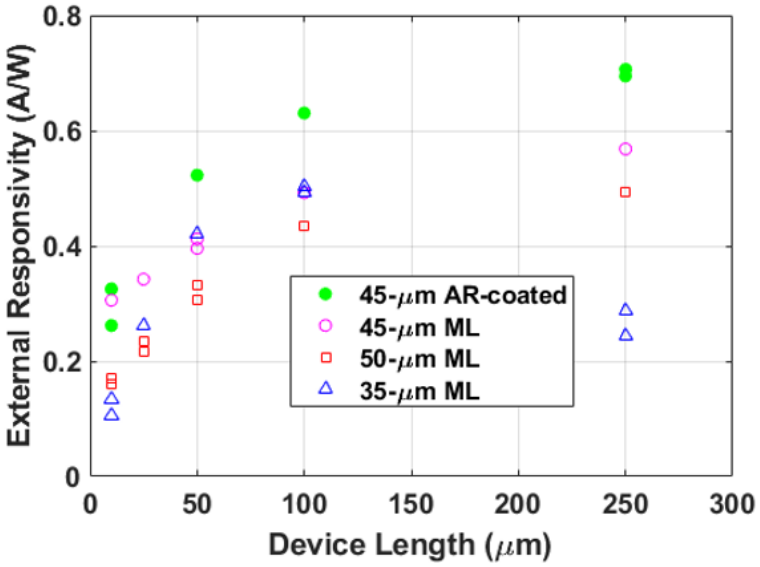

Figure 4-15: Responsivity as a function of device length and matching layer (ML) length, including the AR-coated 45-μm ML devices.

5. Conclusions and Future Work

Overall, this project succeeded in summarizing the current state of InGaAs/InP photodiode technology, characterizing the responsivity and current-handling of the first generation of MIT Lincoln Laboratory Group 89's hybrid photodiodes, and modeling the transmission of light in the photodiode's cavity with MATLAB. The group did not initially anticipate the pad metal at the back of the devices acting as mirrors and resulting in a reflective cavity in the photodiodes. Since increased fluctuation of responsivity as a function of wavelength is undesirable, this project presents the recommendation of AR-coating the photodiodes for integration into microwave photonic systems. This project also provided evidence that even the smallest photodiode in the first generation (active area 2.5×10 μm, designed as the limit to fabrication capabilities) has a responsivity ~ 0.3 A/W, a failure current > 8 mA, and the highest projected 3-dB bandwidth.

While the project was successful in its objectives, questions still remain that could be answered in future work and additional experiments at MIT Lincoln Laboratory. First, the mechanism of the higher frequency oscillations in responsivity as a function of wavelength were investigated, but neither literature nor this work explains the observed oscillations with a period ~10 nm. As a part of this project, responsivity measurements were taken with an increased wavelength range, 1460 – 1640 nm, but the loss in the experimental setup was not calibrated for wavelengths significantly far from 1550 nm. Therefore, this data cannot be considered accurate enough to investigate the nature of the 10-nm oscillations. In the future, calibrating the setup for wavelengths in this increased range would allow for novel insight concerning Group 89's devices and other devices described in the literature. Additional testing is also necessary to determine the mechanism of failure in Group 89's devices. For example, etching away layers of a failed device to reveal the precise location at which the device either shorted or fused would greatly enhance the current-handling data presented in this project.

Additionally, the scope of this 7-week project did not allow for complex modeling in sophisticated tools such as Lumerical. Further modeling of the reflections in the device cavity before and after AR-coating using tools such as FDTD and DEVICE solutions for opto-electronics could be compared to measured data. This would serve as further investigation into the effect that AR-coating has on the responsivity as a function of wavelength.

Lastly, the experimental setup and methods utilized in this project could be applied to testing the second generation of Group 89's InGaAs/InP photodiodes. With the etching correction described in Section 2.3.4, the 3-dB bandwidth of the second generation devices will be measured accurately. These RF tests can confirm whether the smallest fabricated device characterized in this project has the highest bandwidth and greatest speed for system integration. Overall, this collaboration should improve the characterization and performance of Group 89's second generation of devices, and bring the group one step closer to optimized performance in microwave photonic integrated circuits.

6. References

[1] H. Liebe, Average Atmospheric Absorption of Millimeter Waves (n.d.), accessed on 20 August 2018, www.omlinc.com/images/pdf

[2] Zmuda, "Optical Beamforming for Phased Array Antennas," *Adaptive Antenna Arrays* pg. 219-244, Springer-Verlag Berlin Heidelberg, 2004.

[3] A. Beling and J. Campbell, "InP-Based High-Speed Photodetectors," *Journal of Lightwave Technology,* Vol. 27, No. 3 (2009).

[4] T. Nagatsuma, and Y. Kado, "Microwave Photonic Devices and Their Applications to Communications and Measurements," *PIERS Online,* Vol. 4, No. 3 (2008).

[5] G. Zhou, P. Runge, S. Keyvaninia, S. Seifert, W. Ebert, S. Mutschall, A. Seeger, Q. Li, and A. Beling, "High-Power InP-Based Waveguide Integrated Modified Uni-Traveling-Carrier Photodiodes," *Journal of Lightwave Technology,* Vol. 35, No. 4 (2017).

[6] Q. Li, K. Sun, K. Li, Q. Yu, P. Runge, W. Ebert, A. Beling, and J. Campbell, "High-power evanescently coupled waveguide MUTC photodiode with >105-GHz bandwidth," *Journal of Lightwave Technology,* Vol. 35, No. 21 (2017).

[7] L. Coldren, S. Corzine, and M. Mašanović, *Diode Lasers and Photonic Integrated Circuits,* pp. 1-23, Second Edition, John Wiley and Sons, New Jersey: 2012.

[8] M. Achouche, V. Magnin, J. Harari, D. Carpentier, E. Derouin, C. Jany, and D. Decoster, "Design and Fabrication of a p-i-n Photodiode With High Responsivity and Large Alignment Tolerances for 40-Gb/s Applications," *IEEE Photonics Technology Letters,* Vol. 18, No. 4 (2006).

[9] H. Bach, A. Beling, G. Mekonnen, R. Kunkel, D. Schmidt, W. Ebert, A. Seeger, M. Stollberg, and W. Schlaak, "InP-Based Waveguide-Integrated Photodetector with 100-GHz Bandwidth," *IEEE Journal of Selected Topics in Quantum Electronics,* Vol. 10, No. 4 (2004).

[10] K. Williams and R. Esman, "Design Considerations for High-Current Photodetectors," *Journal of Lightwave Technology,* Vol. 17, No. 8 (1999).

[11] J. Shaw, "Radiometry and the Friis transmission equation," *American Journal of Physics,* Vol. 81, No. 33 (2013).

[12] The electromagnetic spectrum (2015), P. Venis, accessed on 20 August 2018, www.infinity-theory.com/en/science/Main_pages/The_Electromagnetic_Spectrum

[13] Semiconductor band gap-lattice constant plot (n.d.), H. Föll, accessed on 30 August 2018, www.tf.uni-kiel.de/matwis/amat/semitech_en/kap_2/backbone/r2_3_1.html

[14] D. Jun, J. Jang, I. Adesida, and J. Song, "Improved Efficiency-Bandwidth Product of Modified Uni-Traveling Carrier Photodiode Structures Using an Undoped Photo-Absorption Layer," *Japanese Journal of Applied Physics,* Vol. 45, No. 4B (2006).

[15] H. Ito, S. Kodama, Y. Muramoto, T. Furuta, T. Nagatsuma, and T. Ishibashi, “High-Speed and High-Output InP-InGaAs Unitraveling-Carrier Photodiodes,” *IEEE Journal of Selected Topics in Quantum Electronics,* Vol. 10, No. 4 (2004).

[16] M. Achouche, V. Magnin, J. Harari, F. Lelarge, E. Derouin, C. Jany, D. Carpentier, F. Blache, and D. Decoster, “High Performance Evanescent Edge Coupled Waveguide Unitraveling-Carrier Photodiodes for >40-Gb/s Optical Receivers,” *IEEE Photonics Technology Letters,* Vol. 16, No. 2 (2004).

[17] E. Rouvalis, M. Chtioui, F. van Dijk, F. Lelarge, M. J. Fice, C.C. Renaud, G. Carpintero, and A.J. Seeds, “170 GHz uni-traveling carrier photodiodes for InP-based photonic integrated circuits,” *Optics Express* Vol. 20, No. 18 20090 (2012).

[18] A. Baranov and E. Tournié, *Semiconductor lasers - Fundamentals and applications,* Woodhead Publishing Limited: 2013.

[19] J. Klamkin, S. Madison, D. Oakley, A. Napoleone, F. O’Donnell, M. Sheehan, L. Missaggia, J. Caissie, J. Plant, and P. Juodawlkis, “Uni-traveling-carrier variable confinement waveguide photodiodes,” *Optics Express* Vol. 19, No. 11 10199 (2011).